Journal of Computational Physics 550 (2026) 114646

Contents lists available at ScienceDirect

Journal of Computational Physics

journal homepage: www.elsevier.com/locate/jcp

Angular-momentum enhanced non-hourglass formulation for SPH solid dynamics

Shuaihao Zhang [a], Jidong Zhao [a], Honghu Zhu [b,c], Xiangyu Hu [d,*]

[a] Department of Civil and Environmental Engineering, Hong Kong University of Science and Technology, Clearwater Bay, Kowloon, Hong Kong SAR, China
[b] School of Earth Sciences and Engineering, Nanjing University, Nanjing, China
[c] Jiangsu Province Engineering Research Center of Earth Sensing and Disaster Control, Nanjing, China
[d] School of Engineering and Design, Technical University of Munich, 85748, Garching, Germany

ARTICLE INFO

Keywords:
Smoothed particle hydrodynamics
Hourglass modes
Solid dynamics
Numerical instability
Updated Lagrangian formulation
Angular momentum conservation

ABSTRACT

Updated Lagrangian smoothed particle hydrodynamics (SPH) for solid dynamics is often plagued by numerical instabilities, particularly hourglass modes that produce unphysical zigzag patterns. While recent essentially non-hourglass (SPH-ENOG) and generalized non-hourglass (SPH-GNOG) formulations have improved stability, they suffer from poor angular momentum conservation, limiting their accuracy in rotational problems. To overcome this, this paper presents two angular-momentum enhanced non-hourglass formulations. First, we enhance the SPH-ENOG method with rotation matrices derived from Rodrigues' formula, creating SPH-ENOG-A for elastic materials, which explicitly accounts for rigid rotations during time integration, thereby significantly enhancing angular momentum conservation. To strictly enforce linear momentum conservation, the average of the rotation matrices is computed and applied to each particle. We then extend this approach to reformulate the corrective term in SPH-GNOG, yielding SPH-GNOG-A—a unified method for both elastic and plastic materials that not only improves angular momentum conservation but also eliminates prior dependencies on material-specific coefficients. Validated against elastic (oscillating plates, spinning solids) and plastic (Taylor bars, high-velocity impacts) benchmarks, our methods retain the hourglass-free stability, convergence, and accuracy of their predecessors while achieving a significant leap in angular momentum conservation.

1. Introduction

Smoothed particle hydrodynamics (SPH) is a meshless Lagrangian method that was initially developed for astrophysical simulations [1,2]. Over the years, SPH has been successfully applied to a wide range of engineering problems, including fluid dynamics [3–6], solid mechanics [7–13], and fluid-structure interactions [14–17]. In the context of solid dynamics, updated Lagrangian smoothed particle hydrodynamics (ULSPH) offers distinct advantages over total Lagrangian smoothed particle hydrodynamics (TL-SPH) for simulating material damage and fracture due to its independence from the initial configuration [18].

However, numerical instabilities, such as zigzag particle and stress distributions, and numerical fractures, frequently arise when employing the original shear force discretization scheme in ULSPH for solid dynamics simulations [7]. These instabilities severely limit the practical application of ULSPH in engineering problems involving large deformations and complex material behavior.

* Corresponding author.
E-mail addresses: shzhangce@ust.hk (S. Zhang), jzhao@ust.hk (J. Zhao), zhh@nju.edu.cn (H. Zhu), xiangyu.hu@tum.de (X. Hu).

https://doi.org/10.1016/j.jcp.2025.114646
Received 18 October 2025; Received in revised form 12 December 2025; Accepted 28 December 2025
Available online 31 December 2025

Initially, Monaghan [19] and Gray et al. [7] attributed particle clustering and non-physical fractures in elastic materials to tensile instability [20]. Gray et al. [7] proposed an artificial stress method that introduces a repulsive force between particle pairs, which increases as interparticle distance decreases, thereby preventing particle clustering. This approach gained widespread adoption in subsequent research. However, while effectively mitigating particle clustering and non-physical fractures, this method produces disordered stress distributions and exhibits zigzag patterns in both stress fields and particle arrangements. These zigzag patterns correspond to a numerical instability known as hourglass modes, previously identified in grid-based methods [21,22] and TLSPH [23,24].

The emergence of hourglass modes stems from zero-energy modes [25], where specific particle velocity distributions (e.g., Fig. 2 in Ref.[26]) generate non-rigid rotational deformations that yield zero strain energy [25,27]. The underlying mechanism involves mutual cancellation of contributions from neighboring particles during first-order derivative calculations (e.g., velocity gradients), leading to erroneous stress estimations. Building on this understanding, Zhang et al. [26] introduced the concept of hourglass modes into ULSPH and addressed numerical instabilities from this perspective. Specifically, drawing inspiration from TLSPH treatments [24], they reformulated shear acceleration into a Laplacian form of velocity, proposing the essentially non-hourglass formulation (SPH-ENOG) [26] to avoid errors inherent in first-order differentiation through second-order derivative computation. Their results demonstrated the elimination of both particle clustering/non-physical fractures and zigzag patterns for elastic simulations, yielding smooth stress fields and uniform particle distributions.

However, extending this methodology to plastic materials with complex constitutive relations remains challenging due to the difficulty in expressing shear acceleration as a second-order velocity derivative for general plasticity models. To address this limitation, Zhang et al. [18] recently proposed the generalized non-hourglass formulation (SPH-GNOG), which introduces a penalty force to correct discrepancies between linearly predicted and actual velocity differences of neighboring particle pairs. Unlike SPH-ENOG's complete reconstruction of the shear acceleration term, SPH-GNOG incorporates the penalty force as a corrective term in the momentum equation. Results confirm SPH-GNOG's effectiveness in eliminating numerical instabilities for both elastic and plastic materials. Nevertheless, Zhang et al. [18] required different modeling coefficients for elastic versus plastic materials, failing to unify this parameter.

An additional limitation concerns the inaccurate maintenance of angular momentum in both SPH-ENOG and SPH-GNOG, which compromises accuracy in scenarios sensitive to angular momentum. SPH-ENOG exhibits severe angular momentum non-conservation due to its complete reformulation of the shear acceleration term [26], while SPH-GNOG's introduction of merely a corrective term results in comparatively minor impacts on overall angular momentum [18]. However, the material-dependent modeling coefficient in SPH-GNOG likely originates from angular momentum non-conservation, as plastic deformations involve more irregular particle rotations that amplify non-conservation effects.

This study consequently investigates angular momentum conservation in ULSPH while maintaining numerical stability for solid material simulations. We first analyze the fundamental causes of angular momentum non-conservation in SPH-ENOG and introduce a rotation matrix to properly reorient shear acceleration at each time step, developing the angular-momentum-enhanced essentially non-hourglass formulation (SPH-ENOG-A). Recognizing SPH-ENOG-A's limitation to elastic materials, we extend the angular momentum correction approach to SPH-GNOG's penalty force, formulating an angular-momentum-enhanced version (SPH-GNOG-A) applicable to both elastic and plastic materials. Although angular momentum non-conservation in SPH-GNOG's corrective term has limited overall impact as noted above, SPH-GNOG-A achieves significant advancement by enabling identical modeling coefficients for elastic and plastic materials, as the correction method significantly mitigates the angular momentum non-conservation inherent to plastic deformation. This eliminates material-dependent parameterization and establishes a unified simulation framework for different constitutive models.

The remainder of this paper is organized as follows: Section 2 outlines the governing equations for elastic and plastic solids. Section 3 describes the fundamental SPH discretization and time integration scheme. Section 4 details the theoretical development of the angular-momentum enhanced formulations. Section 5 presents extensive numerical validation, and Section 6 concludes with key findings and future research directions. For further in-depth research, the algorithms developed in this work have been implemented and open-sourced within the SPHinXsys project [28], available at https://www.sphinxsys.org.

2. Governing equations and constitutive relations

2.1. Elasticity

Within the Lagrangian description, the fundamental conservation laws for mass and momentum governing continuum media are expressed by:

$$\frac{\mathrm{d}\rho}{\mathrm{d}t} = -\rho\nabla\cdot\mathbf{v}, \tag{1}$$

$$\frac{\mathrm{d}\mathbf{v}}{\mathrm{d}t} = \frac{1}{\rho}\nabla\cdot\boldsymbol{\sigma} + \mathbf{g}, \tag{2}$$

where ρ denotes density, $\mathbf{v}$ represents velocity, $\boldsymbol{\sigma}$ is the Cauchy stress tensor, and $\mathbf{g}$ signifies body force per unit mass.

The total stress tensor $\boldsymbol{\sigma}$ admits a decomposition into hydrostatic pressure p and deviatoric shear stress $\boldsymbol{\sigma}^s$:

$$\boldsymbol{\sigma} = -p\mathbf{I} + \boldsymbol{\sigma}^s, \tag{3}$$

with $\mathbf{I}$ as the identity tensor. The hydrostatic pressure is computed via an artificial equation of state [7]:

$$p = c_0^2(\rho - \rho_0), \tag{4}$$

where ρ_0 and ρ correspond to initial and current density, respectively. The sound speed c_0 derives from the bulk modulus K as $c_0 = \sqrt{K/\rho_0}$. This linearized state equation assumes deformation-independent bulk modulus.

Combining (2) and (3), acceleration contributions from volumetric (pressure) and deviatoric (shear) stress components become:

$$\frac{\mathrm{d}\mathbf{v}^p}{\mathrm{d}t} = -\frac{1}{\rho}\nabla p, \tag{5}$$

$$\frac{\mathrm{d}\mathbf{v}^s}{\mathrm{d}t} = \frac{1}{\rho}\nabla \cdot \boldsymbol{\sigma}^s. \tag{6}$$

Here $\frac{\mathrm{d}\mathbf{v}^p}{\mathrm{d}t}$ and $\frac{\mathrm{d}\mathbf{v}^s}{\mathrm{d}t}$ denote pressure-induced and shear-induced acceleration components. The total acceleration $\frac{\mathrm{d}\mathbf{v}}{\mathrm{d}t}$ therefore combines these terms with gravitational effects: $\frac{\mathrm{d}\mathbf{v}}{\mathrm{d}t} = \frac{\mathrm{d}\mathbf{v}^p}{\mathrm{d}t} + \frac{\mathrm{d}\mathbf{v}^s}{\mathrm{d}t} + \mathbf{g}$.

Shear stress evolution follows temporal integration of its rate quantity:

$$\boldsymbol{\sigma}^s = \int_0^t \dot{\boldsymbol{\sigma}}^s \mathrm{d}t. \tag{7}$$

For linear elastic materials, the Jaumann rate of shear stress $\dot{\boldsymbol{\sigma}}^s$ takes the form:

$$\dot{\boldsymbol{\sigma}}^s = 2G\dot{\boldsymbol{\epsilon}}^s + \boldsymbol{\sigma}^s \cdot \boldsymbol{\Omega}^T + \boldsymbol{\Omega} \cdot \boldsymbol{\sigma}^s, \tag{8}$$

where G indicates shear modulus. The deviatoric strain rate $\dot{\boldsymbol{\epsilon}}^s$ relates to the full strain rate $\dot{\boldsymbol{\epsilon}}$ through $\dot{\boldsymbol{\epsilon}}^s = \dot{\boldsymbol{\epsilon}} - \frac{1}{d}\mathrm{tr}(\dot{\boldsymbol{\epsilon}})\mathbf{I}$, with $d = 2, 3$ being spatial dimension and $\mathrm{tr}(\cdot)$ the trace operator. Strain rate $\dot{\boldsymbol{\epsilon}}$ and spin rate $\boldsymbol{\Omega}$ are defined following conventional expressions:

$$\dot{\boldsymbol{\epsilon}} = \tfrac{1}{2}\left[\nabla\mathbf{v} + (\nabla\mathbf{v})^{\mathsf{T}}\right], \tag{9}$$

$$\boldsymbol{\Omega} = \tfrac{1}{2}\left[\nabla\mathbf{v} - (\nabla\mathbf{v})^{\mathsf{T}}\right], \tag{10}$$

where $\nabla\mathbf{v}$ is the velocity gradient tensor and the superscript T denotes transpose.

2.2. Plasticity

The current study employs the J_2 plasticity framework [29], with the yield criterion formulated as:

$$f(J_2, \alpha) = \sqrt{2J_2} - \sqrt{\tfrac{2}{3}}(\kappa\alpha + \sigma_Y). \tag{11}$$

Here $J_2 \equiv \frac{1}{2}\boldsymbol{\sigma}^s : \boldsymbol{\sigma}^s$ represents the second deviatoric stress invariant, where κ denotes the hardening modulus, α is the hardening parameter, and σ_Y signifies the initial yield stress (flow stress).

According to [30], the shear stress evolution in J_2 plasticity follows:

$$\dot{\boldsymbol{\sigma}}^s = 2G\dot{\boldsymbol{\epsilon}}^s - \dot{\lambda}\frac{\sqrt{2}G}{\sqrt{J_2}}\boldsymbol{\sigma}^s + \boldsymbol{\sigma}^s \cdot \boldsymbol{\Omega}^{\mathsf{T}} + \boldsymbol{\Omega} \cdot \boldsymbol{\sigma}^s. \tag{12}$$

The plastic multiplier rate $\dot{\lambda}$ is determined by [30]:

$$\dot{\lambda} = \frac{\boldsymbol{\sigma}^s : \dot{\boldsymbol{\epsilon}}}{(1 + \kappa/3G)\sqrt{2J_2}}. \tag{13}$$

The trial shear stress $\boldsymbol{\sigma}^{s,\mathrm{trial}}$ are first updated based on the stress rate. When the resulting stress violates the yield condition ($f > 0$), a stress return mapping procedure [29,31] enforces consistency by projecting the stress state back onto the yield surface. This correction establishes the following relation between corrected and trial shear stresses [29,31]:

$$\boldsymbol{\sigma}^s = \frac{\kappa\alpha + \sigma_Y}{\sqrt{3J_2^{\mathrm{trial}}}}\boldsymbol{\sigma}^{s,\mathrm{trial}}. \tag{14}$$

3. Method

3.1. SPH discretization

Following standard SPH discretization, the continuity equation becomes:

$$\frac{\mathrm{d}\rho_i}{\mathrm{d}t} = \rho_i \sum_j \mathbf{v}_{ij} \cdot \nabla_i W_{ij} V_j. \tag{15}$$

For the volumetric acceleration term, we adopt a Riemann-based discretization [32,33] of the pressure momentum equation:

$$\frac{\mathrm{d}\mathbf{v}_i^p}{\mathrm{d}t} = -\frac{2}{\rho_i}\sum_j P^* \nabla_i W_{ij} V_j. \tag{16}$$

This study employs the following SPH notations: $W_{ij} \equiv W(\mathbf{r}_i - \mathbf{r}_j, h)$ denotes the kernel function, with $\mathbf{r}$ indicating particle position and h the smoothing length. Subscripts i and j identify particles, while V_j represents the volume of particle j. The unit vector from particle j to i is $\mathbf{e}_{ij}$, and $\mathbf{v}_{ij} = \mathbf{v}_i - \mathbf{v}_j$ gives their relative velocity. The kernel gradient is defined as $\nabla_i W_{ij} = \frac{\partial W(r_{ij},h)}{\partial r_{ij}}\mathbf{e}_{ij}$, where $r_{ij} = |\mathbf{r}_i - \mathbf{r}_j|$ is inter-particle distance.

The Riemann solution P^* [32], obtained along $\mathbf{e}_{ij}$, resolves inter-particle states:

$$P^* = \frac{\rho_L c_L P_R + \rho_R c_R P_L + \rho_L c_L \rho_R c_R (U_L - U_R)}{\rho_L c_L + \rho_R c_R}. \tag{17}$$

Left (L) and right (R) Riemann states are assigned as:

$$\begin{cases} (\rho_L, U_L, P_L, c_L) = (\rho_i, -\mathbf{v}_i \cdot \mathbf{e}_{ij}, p_i, c_{0i}) \\ (\rho_R, U_R, P_R, c_R) = (\rho_j, -\mathbf{v}_j \cdot \mathbf{e}_{ij}, p_j, c_{0j}). \end{cases} \tag{18}$$

The shear-induced acceleration discretizes to:

$$\frac{\mathrm{d}\mathbf{v}_i^s}{\mathrm{d}t} = \frac{1}{\rho_i}\sum_j \left(\boldsymbol{\sigma}_i^s + \boldsymbol{\sigma}_j^s\right) \cdot \nabla_i W_{ij} V_j. \tag{19}$$

The velocity gradient in (9) adopts the discretization [34]:

$$\nabla \mathbf{v}_i = -\sum_j \mathbf{v}_{ij} \otimes \left(\mathbf{B}_i \nabla_i W_{ij}\right) V_j, \tag{20}$$

where the kernel gradient correction matrix $\mathbf{B}_i$ [35,36] is:

$$\mathbf{B}_i = -\left(\sum_j \mathbf{r}_{ij} \otimes \nabla_i W_{ij} V_j\right)^{-1}. \tag{21}$$

3.2. Time integration scheme

To enhance computational efficiency, this study implements the dual-criteria time stepping approach [26,37] with distinct advection (Δt_{ad}) and acoustic (Δt_{ac}) time steps.

The advection step Δt_{ad} updates particle configurations according to:

$$\Delta t_{ad} = \mathrm{CFL}_{ad} \frac{h}{|\mathbf{v}|_{\max}}, \tag{22}$$

where $\mathrm{CFL}_{ad} = 0.2$, h is the smoothing length, and $|\mathbf{v}|_{\max}$ denotes maximum particle advection speed.

For the update of physical variables such as velocity and density, the acoustic time step follows:

$$\Delta t_{ac} = \mathrm{CFL}_{ac} \frac{h}{c_0 + |\mathbf{v}|_{\max}}, \tag{23}$$

where $\mathrm{CFL}_{ac} = 0.4$ and c_0 is the sound speed.

The position-based Verlet scheme [38] is employed for the acoustic time integration, details of which can be found in literatures [18,39].

4. Angular-momentum enhanced non-hourglass formulation

This section first presents a re-derivation of the shear acceleration formulation within the SPH-ENOG framework, yielding an angular-momentum enhanced variant, designated as SPH-ENOG-A. Given that the original SPH-ENOG formulation is restricted to elastic materials, we further extend the derivation methodology to reformulate the penalty force in SPH-GNOG. The resulting SPH-GNOG-A scheme maintains applicability to both elastic and plastic constitutive behaviors.

It is important to note that the proposed non-hourglass formulation is specifically designed to address the hourglass instability within the continuum material. It is not applied to rigid wall interactions, as the contact force calculation (based on the algorithms in SPHinXsys [28]) does not suffer from hourglass modes.

4.1. Angular-momentum enhanced essentially non-hourglass formulation

In the SPH-ENOG, to remove hourglass modes, the second-order derivative of velocity is employed to calculate the shear acceleration, which is expressed as [26]:

$$\frac{\mathrm{d}\mathbf{v}^s}{\mathrm{d}t} = G\frac{1}{\rho}\int_0^t (\nabla^2 \mathbf{v})\mathrm{d}t \tag{24}$$

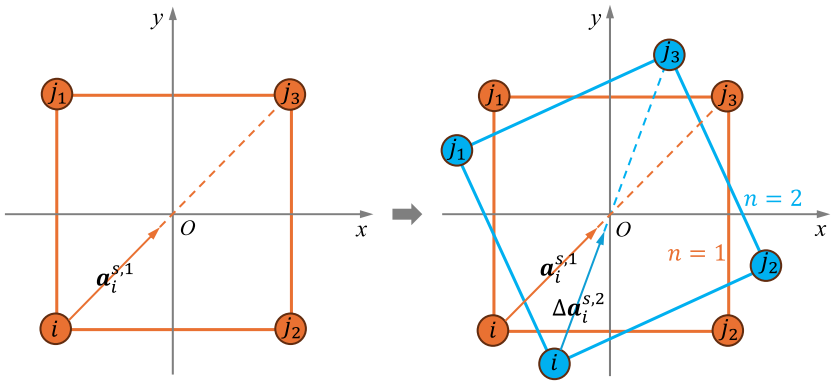

(a) Time step: $n = 1$ (b) Time step: $n = 2$

Fig. 1. Illustration of shear acceleration direction at (a) time step $n = 1$ and (b) time step $n = 2$.

The discrete form of shear acceleration can be written as [26]:

$$\frac{\mathrm{d}\mathbf{v}_i^s}{\mathrm{d}t} = 2\xi_E G \frac{1}{\rho_i} \int_0^t \left(\sum_j \frac{\mathbf{e}_{ij} \cdot \mathbf{v}_{ij}}{r_{ij}} \nabla_i W_{ij} V_j \right) \mathrm{d}t. \tag{25}$$

where ξ_E is a positive parameter related to the smoothing length h and the type of kernel function [40]. According to Zhang et al. [26], the value of ξ_E is set to 3.5 for 2D scenarios and 4.2 for 3D scenarios.

The time integration on the right-hand side of the Eq. (25) signifies that the shear acceleration ($\mathbf{a}^s = \mathrm{d}\mathbf{v}^s/\mathrm{d}t$) is accumulated from the initial time ($t = 0$) up to the current time. Mathematically, this can be expressed as:

$$\mathbf{a}_i^{s,n+1} = \mathbf{a}_i^{s,n} + \Delta\mathbf{a}_i^{s,n+1} \quad n \geq 1. \tag{26}$$

The initial value of $a_i^{s,1}$ at time step $n = 1$ is given by:

$$\mathbf{a}_i^{s,1} = 2\xi_E G \frac{1}{\rho_i} \int_0^{t_1} \left(\sum_j \frac{\mathbf{e}_{ij} \cdot \mathbf{v}_{ij}}{r_{ij}} \nabla_i W_{ij} V_j \right) \mathrm{d}t = 2\xi_E G \underbrace{\frac{1}{\rho_i} \left(\sum_j \frac{\mathbf{e}_{ij} \cdot \mathbf{v}_{ij}}{r_{ij}} \nabla_i W_{ij} V_j \right)}_{n=1} t_1, \tag{27}$$

$\Delta\mathbf{a}_i^{s,n+1}$ is calculated by:

$$\Delta\mathbf{a}_i^{s,n+1} = 2\xi_E G \frac{1}{\rho_i} \int_{t_n}^{t_{n+1}} \left(\sum_j \frac{\mathbf{e}_{ij} \cdot \mathbf{v}_{ij}}{r_{ij}} \nabla_i W_{ij} V_j \right) \mathrm{d}t = 2\xi_E G \underbrace{\frac{1}{\rho_i} \left(\sum_j \frac{\mathbf{e}_{ij} \cdot \mathbf{v}_{ij}}{r_{ij}} \nabla_i W_{ij} V_j \right)}_{n+1} (t_{n+1} - t_n). \tag{28}$$

Although SPH-ENOG is capable of eliminating numerical instabilities in the simulation of elastic materials, its angular momentum conservation is severely compromised. As a result, its computational accuracy decreases in cases where angular momentum plays a significant role [26].

To analyze angular momentum conservation, we consider four particles initially located at the corners of a square and rotating around the center, as illustrated in Fig. 1. In theory, the angular momentum of each particle should remain constant, which requires the net torque $\tau = \mathbf{r} \times \mathbf{F} = m\mathbf{r} \times \mathbf{a}$ acting on each to be zero. Here, $\mathbf{r}$ is the position vector, $\mathbf{F}$ represents the total force, m is the mass, and $\mathbf{a}$ stands for acceleration.

The shear acceleration of particle i at time step $n = 1$ is given by Eq. (27), and the summation is over the three neighboring particles. Each term $\mathbf{a}_{i\to j_k}^{s,1}$ points along the vector connecting i to j_k ($k = 1, 2, 3$). Since $\mathbf{a}_{i\to j_1}^{s,1}$ and $\mathbf{a}_{i\to j_2}^{s,1}$ have equal magnitudes, the resultant shear acceleration $\mathbf{a}_i^{s,1} = \mathbf{a}_{i\to j_1}^{s,1} + \mathbf{a}_{i\to j_2}^{s,1} + \mathbf{a}_{i\to j_3}^{s,1}$ thus aligns with the line joining i and j_3, as depicted in Fig. 1a.

The torque on particle i at this time ($n = 1$) is:

$$\tau_i^1 = m_i \mathbf{r}_i^1 \times \mathbf{a}_i^{s,1}, \tag{29}$$

where the superscript "1" represents the time step $n = 1$. Since $\mathbf{r}_i^1$ and $\mathbf{a}_i^{s,1}$ are collinear, it follows that $\tau_i^1 = 0$. The same result applies to the other particles, indicating that the total angular momentum is preserved at the first time step.

At the subsequent time step $n = 2$, the shear acceleration is updated as:

$$\mathbf{a}_i^{s,2} = 2\xi_E G \frac{1}{\rho_i} \int_0^{t_2} \left(\sum_j \frac{\mathbf{e}_{ij} \cdot \mathbf{v}_{ij}}{r_{ij}} \nabla_i W_{ij} V_j \right) \mathrm{d}t$$

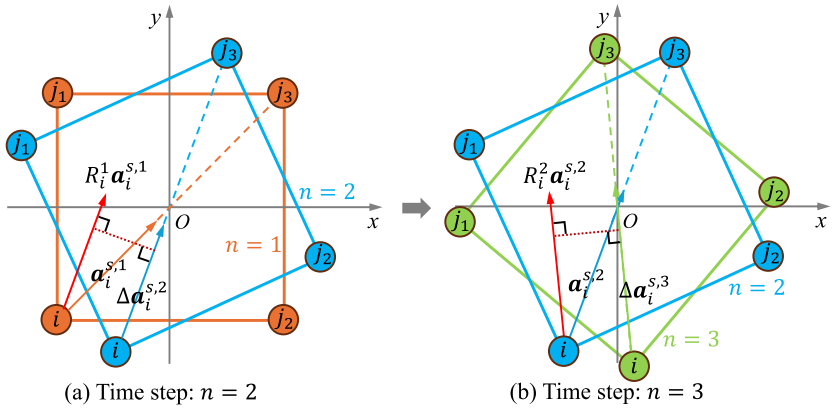

(a) Time step: $n = 2$ (b) Time step: $n = 3$

Fig. 2. Illustrating the direction of shear acceleration after applying a rotation matrix at (a) time step $n = 2$ and (b) time step $n = 3$.

$$
\begin{aligned}
&= 2\xi_E G\frac{1}{\rho_i}\int_0^{t_1}\left(\sum_j \frac{\mathbf{e}_{ij}\cdot\mathbf{v}_{ij}}{r_{ij}}\nabla_i W_{ij}V_j\right)\mathrm{d}t + 2\xi_E G\frac{1}{\rho_i}\int_{t_1}^{t_2}\left(\sum_j \frac{\mathbf{e}_{ij}\cdot\mathbf{v}_{ij}}{r_{ij}}\nabla_i W_{ij}V_j\right)\mathrm{d}t \\
&= 2\xi_E G\underbrace{\frac{1}{\rho_i}\left(\sum_j \frac{\mathbf{e}_{ij}\cdot\mathbf{v}_{ij}}{r_{ij}}\nabla_i W_{ij}V_j\right)}_{n=1}t_1 + 2\xi_E G\underbrace{\frac{1}{\rho_i}\left(\sum_j \frac{\mathbf{e}_{ij}\cdot\mathbf{v}_{ij}}{r_{ij}}\nabla_i W_{ij}V_j\right)}_{n=2}(t_2 - t_1) \\
&= \mathbf{a}_i^{s,1} + \Delta\mathbf{a}_i^{s,2},
\end{aligned}
\tag{30}
$$

where $\Delta\mathbf{a}_i^{s,2}$ denotes the shear acceleration increment. The direction of $\Delta\mathbf{a}_i^{s,2}$ remains aligned with the connection vector between particles i and j_3 at time step $n = 2$ (Fig. 1b), consistent with the directional analysis of $\mathbf{a}_i^{s,1}$. The corresponding torque at $n = 2$ is:

$$
\tau_i^2 = m_i\mathbf{r}_i^2 \times \mathbf{a}_i^{s,2} = m_i\mathbf{r}_i^2 \times \left(\mathbf{a}_i^{s,1} + \Delta\mathbf{a}_i^{s,2}\right) = m_i\mathbf{r}_i^2 \times \mathbf{a}_i^{s,1}, \tag{31}
$$

where the superscript "2" represents the time step $n = 2$. Because the vectors $\mathbf{r}_i^2$ and $\mathbf{a}_i^{s,1}$ are generally not collinear at time step $n = 2$ (as shown in Fig. 1b), $\tau_i(t_1) \neq 0$. Furthermore, calculations show that the torques on all particles (i, j_1, j_2, j_3) point in the same direction. This demonstrates that angular momentum is not conserved in the system at time step $n = 2$.

Prior SPH-ENOG formulations failed to resolve angular momentum non-conservation [26]; this study presents an effective solution to address this fundamental issue. Specifically, we introduce a rotation matrix $\mathbf{R}_i^1$ at time step $n = 2$, which rotates the shear acceleration vector $\mathbf{a}_i^{s,1}$ to align with the direction of $\mathbf{r}_i^2$, as shown in Fig. 2a. The method for calculating the rotation matrix $\mathbf{R}$ will be provided later. At this point, since both $\mathbf{R}_i^1\mathbf{a}_i^{s,1}$ and $\Delta\mathbf{a}_i^{s,2}$ are parallel to $\mathbf{r}_i^2$, the torque of particle i is given by:

$$
\tau_i^2 = m_i\mathbf{r}_i^2 \times \mathbf{a}_i^{s,2} = m_i\mathbf{r}_i^2 \times \underbrace{\left(\mathbf{R}_i^1\mathbf{a}_i^{s,1} + \Delta\mathbf{a}_i^{s,2}\right)}_{\mathbf{a}_i^{s,2}} = 0. \tag{32}
$$

Here, $\mathbf{a}_i^{s,2} = \mathbf{R}_i^1\mathbf{a}_i^{s,1} + \Delta\mathbf{a}_i^{s,2}$ is the shear acceleration at time step $n = 2$ after applying the rotation matrix $\mathbf{R}_i^1$. For the other three particles, the same calculation method shows that their torques are also zero. Therefore, the total torque of the system is zero at $n = 2$, and angular momentum is conserved.

Similarly, at time step $n = 3$ (Fig. 2b), the torque of particle i is given by:

$$
\tau_i^3 = m_i\mathbf{r}_i^3 \times \mathbf{a}_i^{s,3} = m_i\mathbf{r}_i^3 \times \underbrace{\left(\mathbf{R}_i^2\mathbf{a}_i^{s,2} + \Delta\mathbf{a}_i^{s,3}\right)}_{\mathbf{a}_i^{s,3}} = 0. \tag{33}
$$

The total torque of the system is also zero at $n = 3$, and angular momentum is conserved.

Therefore, considering the conservation of angular momentum, the acceleration of particle i caused by shear forces at time step $n + 1$ in SPH-ENOG-A can be expressed as:

$$
\mathbf{a}_i^{s,n+1} = \mathbf{R}_i^n\mathbf{a}_i^{s,n} + \Delta\mathbf{a}_i^{s,n+1} \quad n \geq 1. \tag{34}
$$

The initial value of $a_i^{s,1}$ at time step $n = 1$ is given by Eq. (27).

As the particle moves from one moment to the next, the rotation matrix $\mathbf{R}$ are described by the following differential equation [41]:

$$
\frac{\mathrm{d}\mathbf{R}}{\mathrm{d}t} = \boldsymbol{\Omega}\mathbf{R}, \tag{35}
$$

where the initial value of $\mathbf{R}(0) = \mathbf{I}$. The solution of the above equation takes the form:

$$\mathbf{R} = \exp(\mathbf{\Omega}\Delta t), \tag{36}$$

where $\mathbf{\Omega}$ is the spin rate, and can be calculated by Eq. (10). Δt denotes the time interval between two consecutive time instants. Here, exp denotes the matrix exponential, which can be computed through a Taylor series expansion:

$$\exp(\mathbf{\Omega}\Delta t) = \mathbf{I} + \mathbf{\Omega}\Delta t + \frac{1}{2!}(\mathbf{\Omega}\Delta t)^2 + \frac{1}{3!}(\mathbf{\Omega}\Delta t)^3 + \cdots. \tag{37}$$

Due to the skew-symmetry of $\mathbf{\Omega}$, the series can be simplified into Rodrigues' formula [41,42]:

$$\mathbf{R} = \mathbf{I} + \sin(\|\boldsymbol{\omega}\|\Delta t)\frac{\mathbf{\Omega}}{\|\boldsymbol{\omega}\|} + [1 - \cos(\|\boldsymbol{\omega}\|\Delta t)]\left(\frac{\mathbf{\Omega}}{\|\boldsymbol{\omega}\|}\right)^2, \tag{38}$$

where

$$\|\boldsymbol{\omega}\| = \sqrt{-\frac{1}{2}\mathrm{tr}(\mathbf{\Omega}^2)}. \tag{39}$$

Thus, in Eq. (34), the rotation matrix of particle i at time step n is given by:

$$\mathbf{R}_i^n = \mathbf{I} + \sin(\|\boldsymbol{\omega}_i^n\|\Delta t_{ac}^n)\frac{\mathbf{\Omega}_i^n}{\|\boldsymbol{\omega}_i^n\|} + \left[1 - \cos(\|\boldsymbol{\omega}_i^n\|\Delta t_{ac}^n)\right]\left(\frac{\mathbf{\Omega}_i^n}{\|\boldsymbol{\omega}_i^n\|}\right)^2. \tag{40}$$

The original SPH-ENOG formulation (Eq. (25)) strictly enforces pairwise symmetry in its incremental force calculation, ensuring exact linear momentum conservation. However, this particle-wise rotation $\mathbf{R}_i^n$ inherently relaxes the constraint of strict linear momentum conservation in non-uniformly rotating fields. To overcome this limitation, the average rotation matrix $\overline{\mathbf{R}}^n$ of all particles can be computed and uniformly applied to each particle's shear acceleration update. $\overline{\mathbf{R}}^n$ is defined as:

$$\overline{\mathbf{R}}^n = \frac{1}{N}\sum_{i=1}^{N}\mathbf{R}_i^n, \tag{41}$$

where N is the total number of particles in the system. By doing so, the updated shear acceleration at time step $n+1$ becomes:

$$\mathbf{a}_i^{s,n+1} = \overline{\mathbf{R}}^n\mathbf{a}_i^{s,n} + \Delta\mathbf{a}_i^{s,n+1} \quad n \geq 1. \tag{42}$$

By combining Eqs. (27), (41), and (42), the acceleration of particle i induced by shear forces can be calculated. This approach effectively restores strict linear momentum conservation across the system while still significantly enhancing angular momentum conservation.

It is important to clarify the inherent limitations of the original SPH-ENOG formulation, particularly regarding objectivity and its extension to plasticity. First, in deriving the shear acceleration form (Eq. (25)), the rotational terms from the objective stress rate (i.e., $\boldsymbol{\sigma}^s \cdot \mathbf{\Omega}^T + \mathbf{\Omega} \cdot \boldsymbol{\sigma}^s$) were intentionally neglected to achieve a simplified second-order velocity derivative structure. Consequently, this formulation is not fully objective; it essentially treats the constitutive update as strain-driven without accounting for rigid body rotation, leading to the poor angular momentum conservation observed in rotational benchmarks. Second, the SPH-ENOG approach bypasses the explicit calculation of shear stress in the momentum update. While shear stress is updated for visualization using Eq. (7) and Eq. (8), it does not actively participate in the acceleration calculation. This characteristic renders the original SPH-ENOG unsuitable for plasticity simulations, where explicit stress evaluation is required to check yield criteria and perform return mapping algorithms. These limitations motivated the development of the current angular-momentum enhanced formulation (SPH-ENOG-A) to restore objectivity, and the generalized formulation (SPH-GNOG) to accommodate plasticity.

The complete update procedure for the SPH-ENOG-A formulation, incorporating the rotation matrix and time integration, is summarized in Algorithm 1.

Algorithm 1 Update algorithm for the SPH-ENOG-A formulation.

1: Calculate the initial value of shear acceleration: $\mathbf{a}_i^{s,1} = 2\xi_E G \underbrace{\frac{1}{\rho_i}\left(\sum_j \frac{\mathbf{e}_{ij}\cdot\mathbf{v}_{ij}}{r_{ij}}\nabla_i W_{ij}V_j\right)}_{n=1} t_1$.

2: Compute shear acceleration increment: $\Delta\mathbf{a}_i^{s,n+1} = 2\xi_E G \underbrace{\frac{1}{\rho_i}\left(\sum_j \frac{\mathbf{e}_{ij}\cdot\mathbf{v}_{ij}}{r_{ij}}\nabla_i W_{ij}V_j\right)}_{n+1}(t_{n+1} - t_n)$.

3: Construct rotation matrix: $\mathbf{R}_i^n = \mathbf{I} + \sin(\|\boldsymbol{\omega}_i^n\|\Delta t_{ac}^n)\frac{\mathbf{\Omega}_i^n}{\|\boldsymbol{\omega}_i^n\|} + \left[1 - \cos(\|\boldsymbol{\omega}_i^n\|\Delta t_{ac}^n)\right]\left(\frac{\mathbf{\Omega}_i^n}{\|\boldsymbol{\omega}_i^n\|}\right)^2$.

4: Calculate average rotation matrix: $\overline{\mathbf{R}}^n = \frac{1}{N}\sum_{i=1}^{N}\mathbf{R}_i^n$.

5: Update total shear acceleration at step $n+1$: $\mathbf{a}_i^{s,n+1} = \overline{\mathbf{R}}^n\mathbf{a}_i^{s,n} + \Delta\mathbf{a}_i^{s,n+1} \quad n \geq 1$.

4.2. Angular-momentum enhanced generalized non-hourglass formulation

In SPH-GNOG, a penalty force is incorporated into the momentum equation to address the hourglass modes [18]. The penalty force is defined as:

$$\hat{\mathbf{f}}_i = \xi_G G \int_0^t \left(\sum_j \frac{\hat{\mathbf{v}}_{ij}}{\left|\mathbf{r}_{ij}\right|} \frac{\partial W_{ij}}{\partial r_{ij}} V_i V_j \right) \mathrm{d}t. \tag{43}$$

The time integration term $\int_0^t (\bullet)\mathrm{d}t$ indicates that the penalty force at point i is computed as the cumulative contribution of the integrand, represented by $\bullet$, from the initial time ($t = 0$) to the current time. $\hat{\mathbf{v}}_{ij}$ represents the error value between the actual velocity difference and the linearly predicted velocity difference, defined as [18]:

$$\hat{\mathbf{v}}_{ij} = \mathbf{v}_{ij} - \mathbf{v}_{ij}^{linear} = \mathbf{v}_{ij} - \frac{1}{2}\left(\nabla \mathbf{v}_i + \nabla \mathbf{v}_j\right) \cdot \mathbf{r}_{ij}. \tag{44}$$

The acceleration of particle i caused by the penalty force is $\hat{\mathbf{a}}_i = \hat{\mathbf{f}}_i / m_i$. Subsequently, $\hat{\mathbf{a}}_i$ is introduced into the original momentum equation Eq. (19) to calculate the shear acceleration, to remove the hourglass modes.

$$\frac{\mathrm{d}\mathbf{v}_i^s}{\mathrm{d}t} = \frac{1}{\rho_i} \sum_j \left(\boldsymbol{\sigma}_i^s + \boldsymbol{\sigma}_j^s \right) \cdot \nabla_i W_{ij} V_j + \hat{\mathbf{a}}_i. \tag{45}$$

The above formula represents the method used in SPH-GNOG to compute the shear acceleration.

However, in SPH-GNOG, the coefficient ξ_G must differ between elastic and plastic materials, likely because the correction term $\hat{\mathbf{a}}_i$ in Eq. (45) does not guarantee angular momentum conservation. In this study, following the approach in Section 4.1, a rotation matrix $\mathbf{R}$ is introduced in SPH-GNOG to enhance the angular momentum conservation of $\hat{\mathbf{a}}_i$.

First, following the derivation process in SPH-ENOG [26], the penalty force is projected onto the direction of $\mathbf{e}_{ij}$, which is expressed as:

$$\hat{\mathbf{f}}_i = \xi_G G \int_0^t \left(\sum_j \frac{\hat{\mathbf{v}}_{ij} \cdot \mathbf{e}_{ij}}{\left|\mathbf{r}_{ij}\right|} \nabla_i W_{ij} V_i V_j \right) \mathrm{d}t. \tag{46}$$

Then, analogous to Eq. (34), at time step $n+1$, the value of $\hat{\mathbf{a}}_i$ is given as:

$$\hat{\mathbf{a}}_i^{n+1} = \overline{\mathbf{R}}^n \hat{\mathbf{a}}_i^n + \Delta \hat{\mathbf{a}}_i^{n+1} \quad n \geq 1. \tag{47}$$

The initial value of $\hat{\mathbf{a}}_i^1$ is given by:

$$\hat{\mathbf{a}}_i^1 = \xi_G G \frac{1}{\rho_i} \int_0^{t_1} \left(\sum_j \frac{\hat{\mathbf{v}}_{ij} \cdot \mathbf{e}_{ij}}{\left|\mathbf{r}_{ij}\right|} \nabla_i W_{ij} V_j \right) \mathrm{d}t = \xi_G G \underbrace{\frac{1}{\rho_i} \left(\sum_j \frac{\hat{\mathbf{v}}_{ij} \cdot \mathbf{e}_{ij}}{\left|\mathbf{r}_{ij}\right|} \nabla_i W_{ij} V_j \right)}_{n=1} t_1. \tag{48}$$

$\Delta \hat{\mathbf{a}}_i^{n+1}$ is calculated by:

$$\Delta \hat{\mathbf{a}}_i^{n+1} = \xi_G G \int_{t_n}^{t_{n+1}} \left(\sum_j \frac{\hat{\mathbf{v}}_{ij} \cdot \mathbf{e}_{ij}}{\left|\mathbf{r}_{ij}\right|} \nabla_i W_{ij} V_i V_j \right) \mathrm{d}t = \xi_G G \underbrace{\frac{1}{\rho_i} \left(\sum_j \frac{\hat{\mathbf{v}}_{ij} \cdot \mathbf{e}_{ij}}{\left|\mathbf{r}_{ij}\right|} \nabla_i W_{ij} V_i V_j \right)}_{n+1} (t_{n+1} - t_n). \tag{49}$$

The rotation matrix $\overline{\mathbf{R}}^n$ is computed via the same procedure as in Eq. (40) and Eq. (41). With this approach, the proposed SPH-GNOG-A ensures a consistent coefficient of $\xi_G = 2$ for both elastic and plastic materials.

The update procedure for the SPH-GNOG-A formulation is summarized in Algorithm 2.

5. Numerical examples

In this section, we assess a series of benchmark problems and compare the outcomes against analytical solutions and previously reported numerical results, both qualitatively and quantitatively. For clarity, we adopt the following abbreviations for the SPH formulations considered in this study: SPH-OG denotes the original ULSPH method; SPH-OAS, the original ULSPH with artificial stress [7]; SPH-ENOG, the essentially non-hourglass ULSPH formulation [26]; SPH-GNOG, the generalized non-hourglass ULSPH formulation [18]; SPH-ENOG-A, the proposed essentially non-hourglass ULSPH with angular-momentum enhancement; and SPH-GNOG-A, the proposed generalized non-hourglass ULSPH with angular-momentum enhancement.

In this study, all simulations employ the 5th-order Wendland kernel [43] with smoothing length $h = 1.3dp$ and cut-off radius $2.6dp$, where dp denotes the initial particle spacing. The modeling coefficients ξ_E (3.5 for 2D cases and 4.2 for 3D cases) and ξ_G (2.0) were determined empirically through systematic numerical calibration experiments, and these values are kept constant across all cases presented in this study. Incorporation of the kernel gradient correction [24,44,45] into the governing equations is expected to further enhance accuracy and convergence. This will be investigated in future work and is beyond the scope of the present study.

Algorithm 2 Update algorithm for the SPH-GNOG-A formulation.

1: Calculate the initial value of acceleration induced by penalty force: $\hat{\mathbf{a}}_i^1 = \xi_G G \underbrace{\frac{1}{\rho_i}\left(\sum_j \frac{\hat{\mathbf{v}}_{ij}\cdot\mathbf{e}_{ij}}{|\mathbf{r}_{ij}|}\nabla_i W_{ij} V_j\right)}_{n=1} t_1$.

2: Compute the increment of acceleration induced by penalty force: $\Delta\hat{\mathbf{a}}_i^{n+1} = \xi_G G \underbrace{\frac{1}{\rho_i}\left(\sum_j \frac{\hat{\mathbf{v}}_{ij}\cdot\mathbf{e}_{ij}}{|\mathbf{r}_{ij}|}\nabla_i W_{ij} V_i V_j\right)}_{n+1}(t_{n+1}-t_n)$.

3: Construct rotation matrix: $\mathbf{R}_i^n = \mathbf{I} + \sin(\|\boldsymbol{\omega}_i^n\|\Delta t_{ac}^n)\frac{\boldsymbol{\Omega}_i^n}{\|\boldsymbol{\omega}_i^n\|} + \left[1-\cos(\|\boldsymbol{\omega}_i^n\|\Delta t_{ac}^n)\right]\left(\frac{\boldsymbol{\Omega}_i^n}{\|\boldsymbol{\omega}_i^n\|}\right)^2$.

4: Calculate average rotation matrix: $\overline{\mathbf{R}}^n = \frac{1}{N}\sum_{i=1}^N \mathbf{R}_i^n$.

5: Compute the acceleration induced by penalty force at step $n+1$: $\hat{\mathbf{a}}_i^{n+1} = \overline{\mathbf{R}}^n\hat{\mathbf{a}}_i^n + \Delta\hat{\mathbf{a}}_i^{n+1} \quad n \geq 1$.

6: Update the total shear acceleration at step $n+1$: $\mathbf{a}_i^{s,n+1} = \underbrace{\frac{1}{\rho_i}\sum_j\left(\boldsymbol{\sigma}_i^s + \boldsymbol{\sigma}_j^s\right)\cdot\nabla_i W_{ij} V_j}_{n+1} + \hat{\mathbf{a}}_i^{n+1}$.

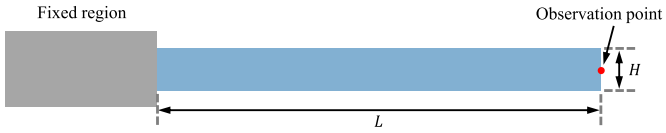

Fig. 3. 2D oscillating plate: model setup.

5.1. Elastic examples

This subsection evaluates the stability, convergence, and accuracy of the proposed SPH-ENOG-A and SPH-GNOG-A formulations via a series of elastic solid dynamics benchmarks, assessing their performance across various deformation scenarios.

5.1.1. 2D oscillating plate

A 2D elastic plate of length L and thickness H is clamped at the left edge, forming a cantilever (Fig. 3) [7,26,39,46]. Numerical results are compared against classical theory [47] and prior computations [7,18,26]. An observation point is placed at the mid-span of the free end to record the vertical deflection, defined as positive upward.

A transverse initial velocity is prescribed as:

$$v_y(x) = v_f\, c_0\, \frac{f(x)}{f(L)}, \tag{50}$$

with the mode shape:

$$f(x) = (\sin(kL)+\sinh(kL))(\cos(kx)-\cosh(kx)) - (\cos(kL)+\cosh(kL))(\sin(kx)-\sinh(kx)), \tag{51}$$

where v_f is a user-specified amplitude, c_0 is the sound speed, and $kL = 1.875$ is the first-mode root of $\cos(kL)\cosh(kL) = -1$.

The theoretical natural frequency is:

$$\omega^2 = \frac{EH^2k^4}{12\,\rho_0\left(1-\nu^2\right)}, \tag{52}$$

where E is Young's modulus and ν is Poisson's ratio. Material and geometric parameters follow [7,48]: $\rho_0 = 1000\,\mathrm{kg/m^3}$, $E = 2\times10^6$ Pa, $\nu = 0.3975$, $L = 0.2$ m, and $H = 0.02$ m.

Fig. 4 presents a comparative analysis of the von Mises stress distribution and particle arrangement in the 2D oscillating plate simulation at various time steps, employing different numerical schemes. Fig. 4a, corresponding to the original SPH formulation without hourglass control (SPH-OG) [26], exhibits severe numerical pathologies, including non-physical fracture formation and disordered particle patterns, indicative of strong numerical instabilities. The outcome from SPH-OAS [26], shown in Fig. 4b, demonstrates a marked improvement by preventing fracture formation; however, a pronounced zigzag stress pattern and particle disorder emerge over time ($t = 0.37$ s), reflecting the accumulation of spurious numerical modes. In contrast, both the SPH-ENOG (Fig. 4c) and SPH-GNOG (Fig. 4d) formulations produce numerically stable results, characterized by smooth stress transitions and a well-ordered particle configuration throughout the simulation. The proposed angular-momentum enhancing variants, SPH-ENOG-A (Fig. 4e) and SPH-GNOG-A (Fig. 4f), yield outcomes of equally high quality-displaying uniform particle distributions and physically plausible stress fields.

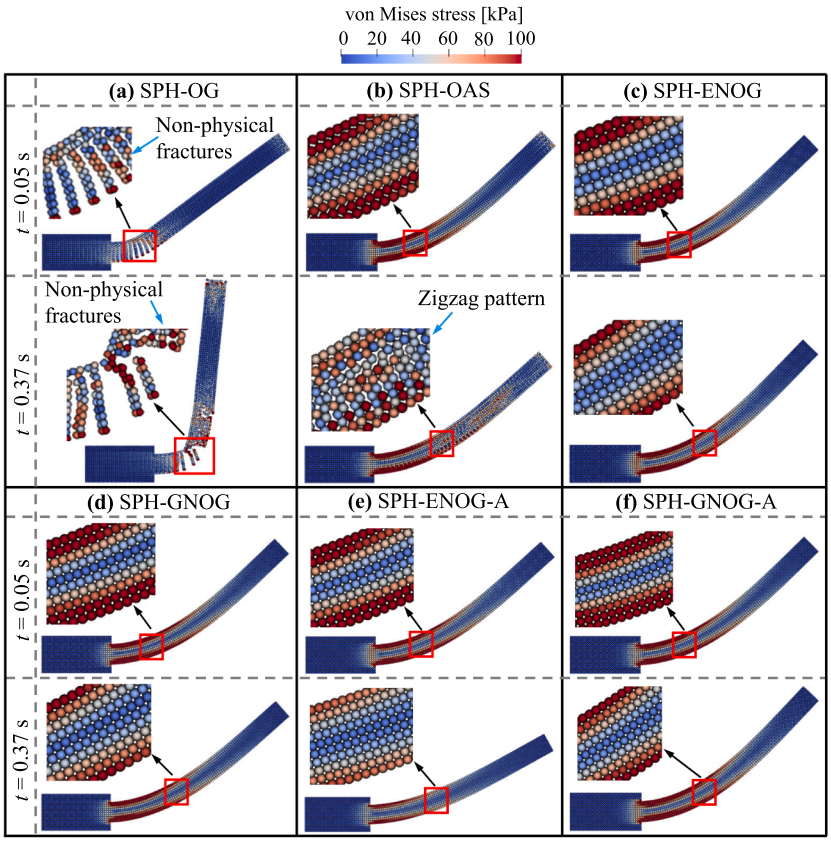

Fig. 4. 2D oscillating plate: evolution of particle configuration with time ($t = 0.05$ s and 0.37 s) for (a) SPH-OG [26], (b) SPH-OAS [7,26], (c) SPH-ENOG [26], and, (d) SPH-GNOG [18], (e) SPH-ENOG-A, and (f) SPH-GNOG-A. Here, $v_f = 0.05\,\mathrm{m/s}$. The particles are colored by von Mises stress.

Fig. 5 presents a convergence study of the proposed SPH-ENOG-A and SPH-GNOG-A formulations. Subfigures (a) and (b) depict the temporal evolution of deflection at three different spatial resolutions ($H/dp = 10$, 20, and 40). The deflection curves demonstrate diminishing discrepancies between adjacent resolutions as the resolution is refined, demonstrating the convergence behavior of both methods-a finding consistent with established literatures [7,16,24,48]. Subfigures (c) and (d) present a quantitative convergence analysis based on the error relative to the reference solution at the finest resolution ($H/dp = 40$). The convergence rates, calculated from the error norms between solutions at $H/dp = 10$, $H/dp = 20$ and the reference, are approximately 1.5 for both SPH-ENOG-A and SPH-GNOG-A.

Furthermore, the predictive capability of the proposed formulations is quantitatively assessed. Table 1 compares the computed first oscillation periods of the 2D oscillating plate against theoretical values across a range of initial velocities, including results from multiple established SPH schemes such as the transport-velocity formulation (SPH-TVF) [46] and the unified transport-velocity formulation (SPH-UTVF) [46]. The newly developed SPH-ENOG-A and SPH-GNOG-A demonstrate errors comparable to those of existing approaches, with the latter showing particularly consistent performance independent of the initial velocity magnitude. This comparison confirms that the proposed methods achieve numerical accuracy on par with state-of-the-art SPH formulations for solid dynamics. It is worth noting that in this particular benchmark, where angular momentum conservation is less critical, both SPH-ENOG and SPH-GNOG are capable of delivering accurate results, similar to those achieved by their angular-momentum enhancing counterparts, SPH-ENOG-A and SPH-GNOG-A. It should be noted that SPH-ENOG-A is limited to elastic constitutive models. In contrast, SPH-GNOG-A offers unified applicability to both elastic and plastic materials, providing enhanced versatility for practical engineering simulations involving complex material responses.

Fig. 6 illustrates the long-term stability of three SPH schemes evaluated through an extended simulation spanning over 30 oscillation periods, with all methods employing a single time-step size to minimize accumulated integration errors. While SPH-OAS exhibits rapid amplitude attenuation, indicating excessive numerical dissipation, both proposed formulations (SPH-ENOG-A and SPH-GNOG-A) maintain stable oscillation amplitudes with only minimal decay. Furthermore, pronounced hourglass modes emerge in SPH-OAS at later stages, whereas the proposed formulations preserve smooth stress distributions and uniform particle arrangements throughout the entire simulation duration, demonstrating superior numerical stability for long-term dynamics.

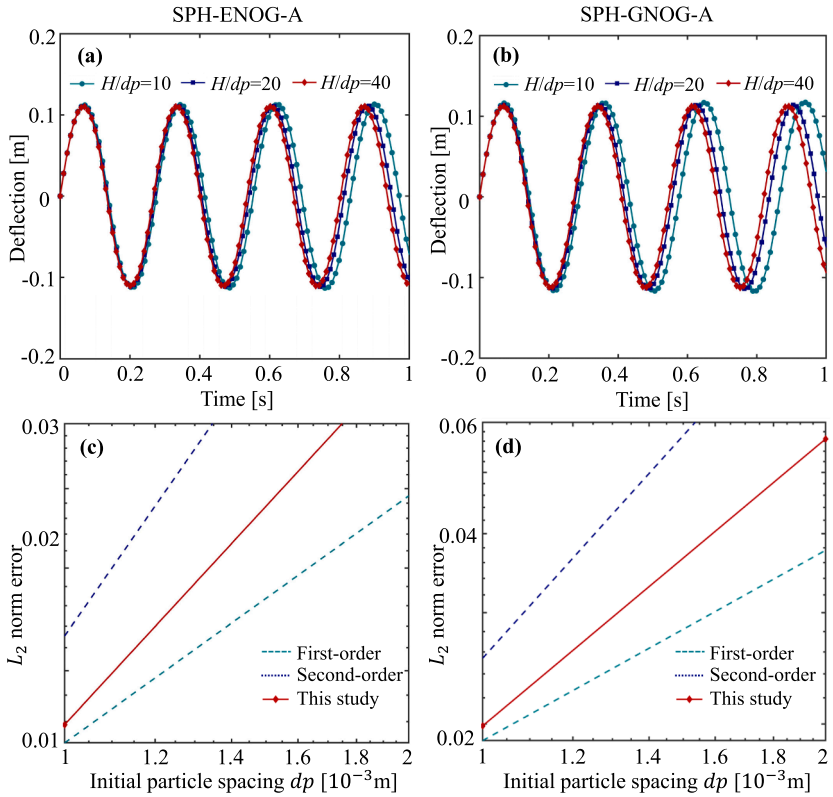

Fig. 5. 2D oscillating plate: convergence study of the proposed SPH-ENOG-A and SPH-GNOG-A; (a)-(b) temporal evolution of deflection at various resolutions; (c)-(d) convergence analysis. $v_f = 0.05\,\mathrm{m/s}$.

Table 1
2D oscillating plate: comparison of the first oscillation period T obtained from the present SPH-ENOG-A and SPH-GNOG-A formulations, various existing SPH methods (SPH-OAS [7], SPH-TVF [46], SPH-UTVF [46], SPH-ENOG [26], SPH-GNOG [18]), and analytical solutions. Here, $L = 0.2$, $H = 0.02$ and $H/dp = 30$.

v_f	0.001	0.01	0.03	0.05
T (Analytical)	0.254	0.254	0.254	0.254
T (SPH-OAS [7])	0.273	0.273	0.275	0.278
T (SPH-TVF [46])	0.275	0.277	0.283	0.284
T (SPH-UTVF [46])	0.274	0.271	0.271	0.271
T (SPH-ENOG [26])	0.262	0.263	0.268	0.279
T (SPH-GNOG [18])	0.275	0.273	0.272	0.272
T (SPH-ENOG-A)	0.265	0.265	0.266	0.269
T (SPH-GNOG-A)	0.274	0.274	0.274	0.275

The first oscillation period T for the 2D oscillating plate, obtained using different cut-off radii, is presented in Table 2. The results demonstrate minimal variation in T across the tested range. This indicates that the chosen cut-off radius is sufficient for solution convergence. Furthermore, the consistency observed across all radii confirms that the current modeling coefficients (ξ_E and ξ_G) remain applicable for different kernel supports.

5.1.2. 3D oscillating plate

This section examines the oscillatory behavior of a 3D thin plate under simply-supported boundary conditions applied along all four lateral edges. As illustrated in Fig. 7, the model consists of an elastic plate with dimensions $L = W = 0.4\,\mathrm{m}$ and thickness $H = 0.01\,\mathrm{m}$, following established benchmarks in the literature [15,24,49]. The simply-supported condition is enforced by constraining the out-of-plane displacement (i.e., along the z-direction) of particles located at the midpoints of each side. An observation point is placed at the plate center to record vertical deflections over time.

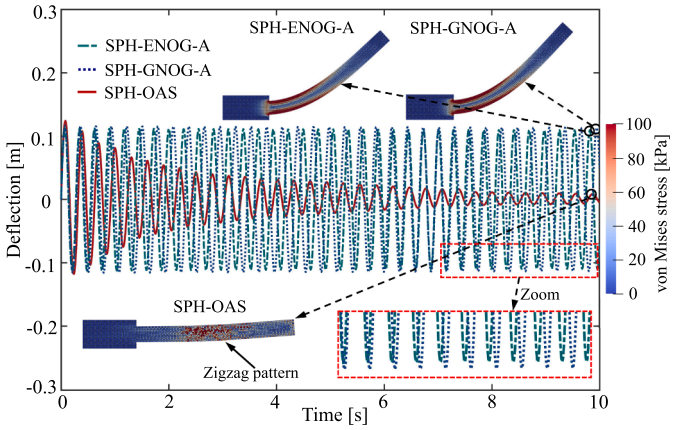

Fig. 6. 2D oscillating plate: long-term stability assessment of SPH-ENOG-A and SPH-GNOG-A formulations compared with SPH-OAS [26]. $H/dp = 10$ and $v_f = 0.05\,\mathrm{m/s}$.

Table 2
2D oscillating plate: comparison of the first oscillation period T calculated using different cut-off radii.

Method	Cut-off radius	v_f			
		0.001	0.01	0.03	0.05
T (SPH-ENOG-A)	$2.6dp$	0.265	0.265	0.266	0.269
	$2.8dp$	0.265	0.265	0.267	0.270
	$3.0dp$	0.267	0.266	0.269	0.271
T (SPH-GNOG-A)	$2.6dp$	0.274	0.274	0.274	0.275
	$2.8dp$	0.273	0.273	0.274	0.274
	$3.0dp$	0.273	0.273	0.273	0.273

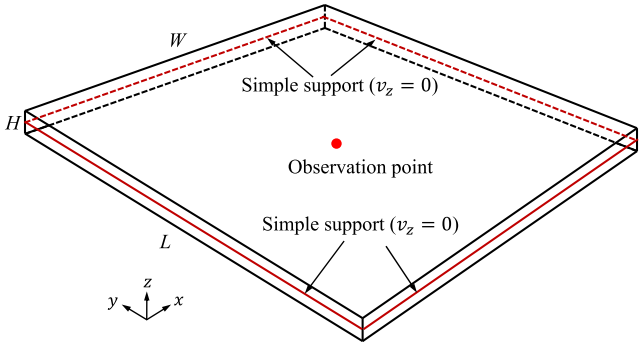

Fig. 7. 3D oscillating plate: model setup.

The plate is initialized with a velocity field in the z-direction defined as:

$$v_z(x, y) = \sin\left(\frac{m\pi x}{L}\right)\sin\left(\frac{n\pi y}{W}\right), \tag{53}$$

where m and n are modal integers governing the vibration shape in the x- and y-directions, respectively.

The theoretical oscillation period for this configuration is given by:

$$T = \frac{2}{\pi}\left[\left(\frac{m}{L}\right)^2 + \left(\frac{n}{W}\right)^2\right]^{-1}\sqrt{\frac{\rho_0 H}{D}}, \tag{54}$$

where D denotes the flexural rigidity, calculated as:

$$D = \frac{EH^3}{12(1-\nu^2)}. \tag{55}$$

The material properties are assigned as follows: density $\rho_0 = 1000\,\mathrm{kg/m^3}$, Young's modulus $E = 1\times10^8$ Pa, and Poisson's ratio $\nu = 0.3$.

The particle distribution and von Mises stress profile are first examined to assess the numerical stability of the proposed formulations. Fig. 8 illustrates the deformed configurations and stress distributions obtained using SPH-ENOG-A and SPH-GNOG-A at

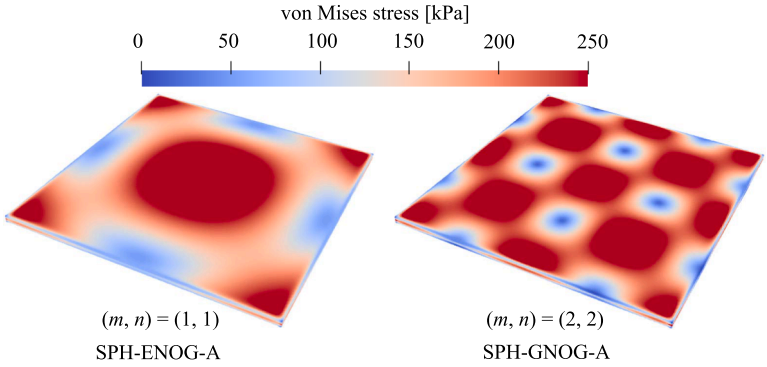

Fig. 8. 3D oscillating plate: deformed configurations from SPH-ENOG-A and SPH-GNOG-A at $t = 0.01$ s for vibration modes $(m, n) = (1, 1)$ and $(2, 2)$, respectively ($H/dp = 9$).

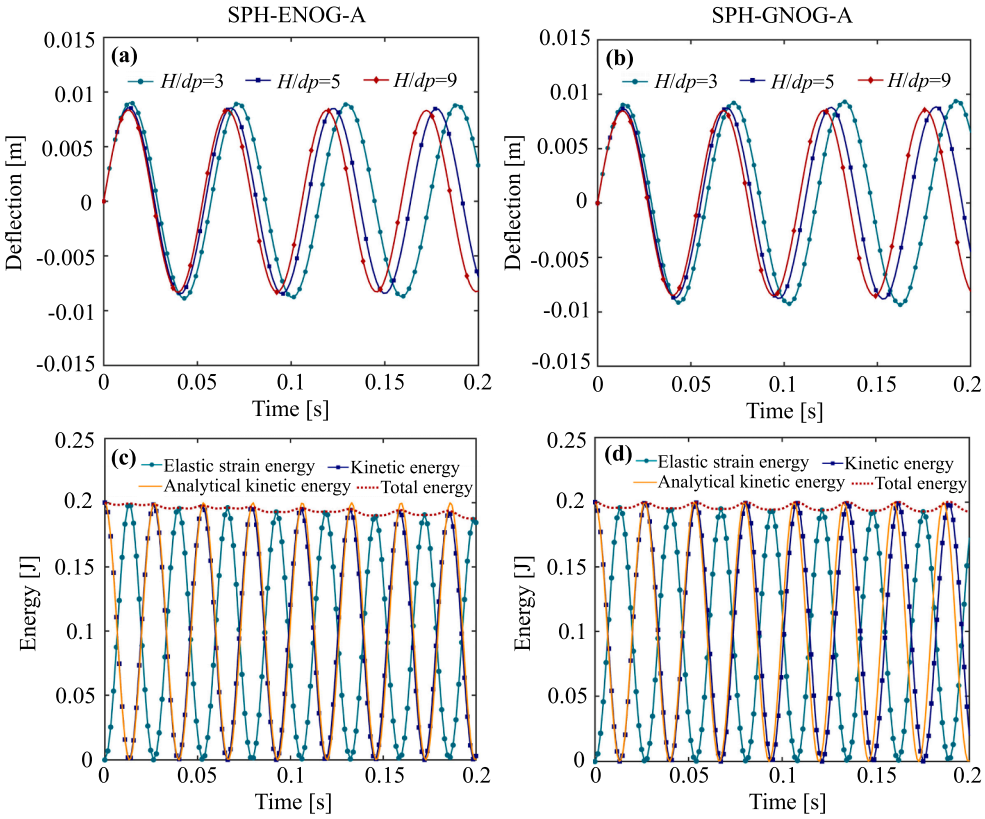

Fig. 9. 3D oscillating plate: (a)-(b) time histories of deflection under different initial particle spacings (dp) for SPH-ENOG-A and SPH-GNOG-A; (c)-(d) temporal evolution of elastic strain energy, kinetic energy, and total energy for SPH-ENOG-A and SPH-GNOG-A ($H/dp = 9$). All cases correspond to mode $(m, n) = (1, 1)$.

$t = 0.01$ s for vibration modes $(m, n) = (1, 1)$ and $(2, 2)$. Both schemes produce smooth stress profiles and maintain uniform particle distributions without non-physical fractures or hourglass instabilities, demonstrating their robustness in handling complex deformation modes. Fig. 9 presents the time history of deflection and energy evolution for both SPH-ENOG-A and SPH-GNOG-A. Subfigures (a) and (b) show that the deflection curves converge consistently as the resolution increases (i.e., decreasing initial particle spacing dp), indicating the spatial convergence of the proposed methods. Subfigures (c) and (d) depict the evolution of elastic strain energy, kinetic energy, and total energy over time. Although minor fluctuations are observed due to numerical effects, the total energy exhibits a gradually decaying trend-consistent with the numerical dissipation inherent in the Riemann solver employed. In addition, we plan to incorporate entropy-stable methods in future work, following established frameworks [50–52], to enforce non-negativity of entropy production. This is expected to eliminate the energy oscillations and ensure a monotonic decay of the total system energy.

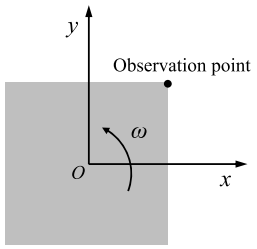

Fig. 10. 2D spinning plate: model setup.

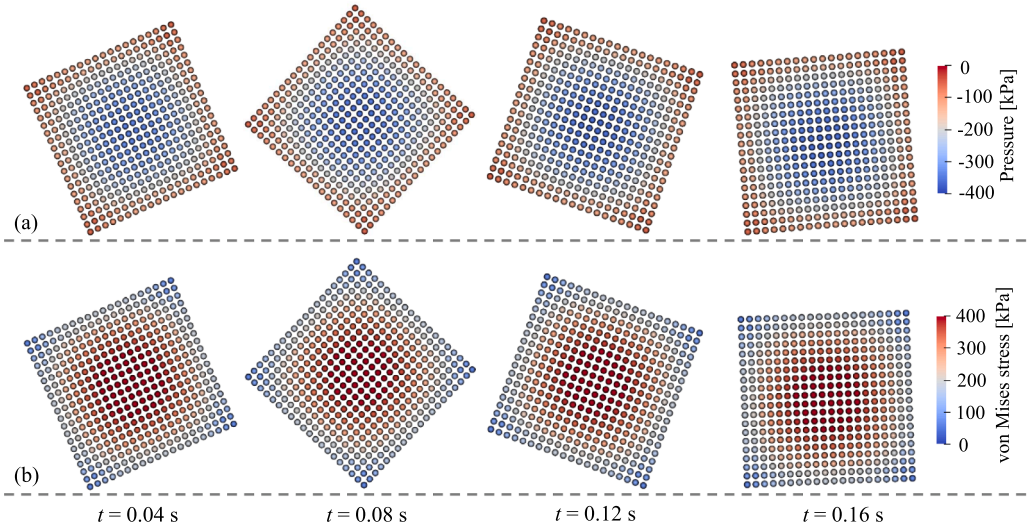

Fig. 11. 2D spinning plate: evolution of particle configuration at different instants for (a) SPH-ENOG-A, colored by pressure, and (b) SPH-GNOG-A, colored by von Mises stress.

Table 3
3D oscillating plate: comparison of the first oscillation period T obtained by SPH-ENOG-A, SPH-GNOG-A and analytical solutions for different vibration modes (m, n) and resolutions.

Method	(m, n)	Oscillation Period T			Analytical
		$H/dp = 3$	$H/dp = 5$	$H/dp = 9$	
SPH-ENOG-A	(1, 1)	0.0573	0.0543	0.0528	0.0532
	(2, 1)	0.0231	0.0218	0.0212	0.0213
	(2, 2)	0.0149	0.0141	0.0136	0.0133
SPH-GNOG-A	(1, 1)	0.0581	0.0553	0.0538	0.0532
	(2, 1)	0.0241	0.0226	0.0220	0.0213
	(2, 2)	0.0153	0.0144	0.0138	0.0133

Furthermore, the first oscillation periods under different vibration modes and resolutions are summarized in Table 3. The results confirm that both SPH-ENOG-A and SPH-GNOG-A yield period values that converge toward the theoretical solution as resolution increases. At the highest resolution considered ($H/dp = 9$), the maximum error across all vibration modes remains below 4%, underscoring the accuracy and convergence of the proposed methods.

5.1.3. 2D spinning plate

To evaluate the capability of the proposed algorithm in suppressing numerical instabilities under tension-dominated conditions, a 2D elastic spinning plate case is considered [18,39,53]. As depicted in Fig. 10, a square plate of unit side length (1 m) is initialized with a rigid-body rotation about its center at an angular velocity $\omega = 50$ rad/s, in the absence of initial deformation or external constraints. Under these ideal conditions, both linear and angular momentum are theoretically conserved. While the preceding benchmarks focused on non-rotational scenarios, this case specifically examines the angular momentum conservation properties of the proposed SPH-ENOG-A and SPH-GNOG-A formulations. Material properties are defined as [54]: initial density $\rho_0 = 1100\,\mathrm{kg/m^3}$, Young's mod-

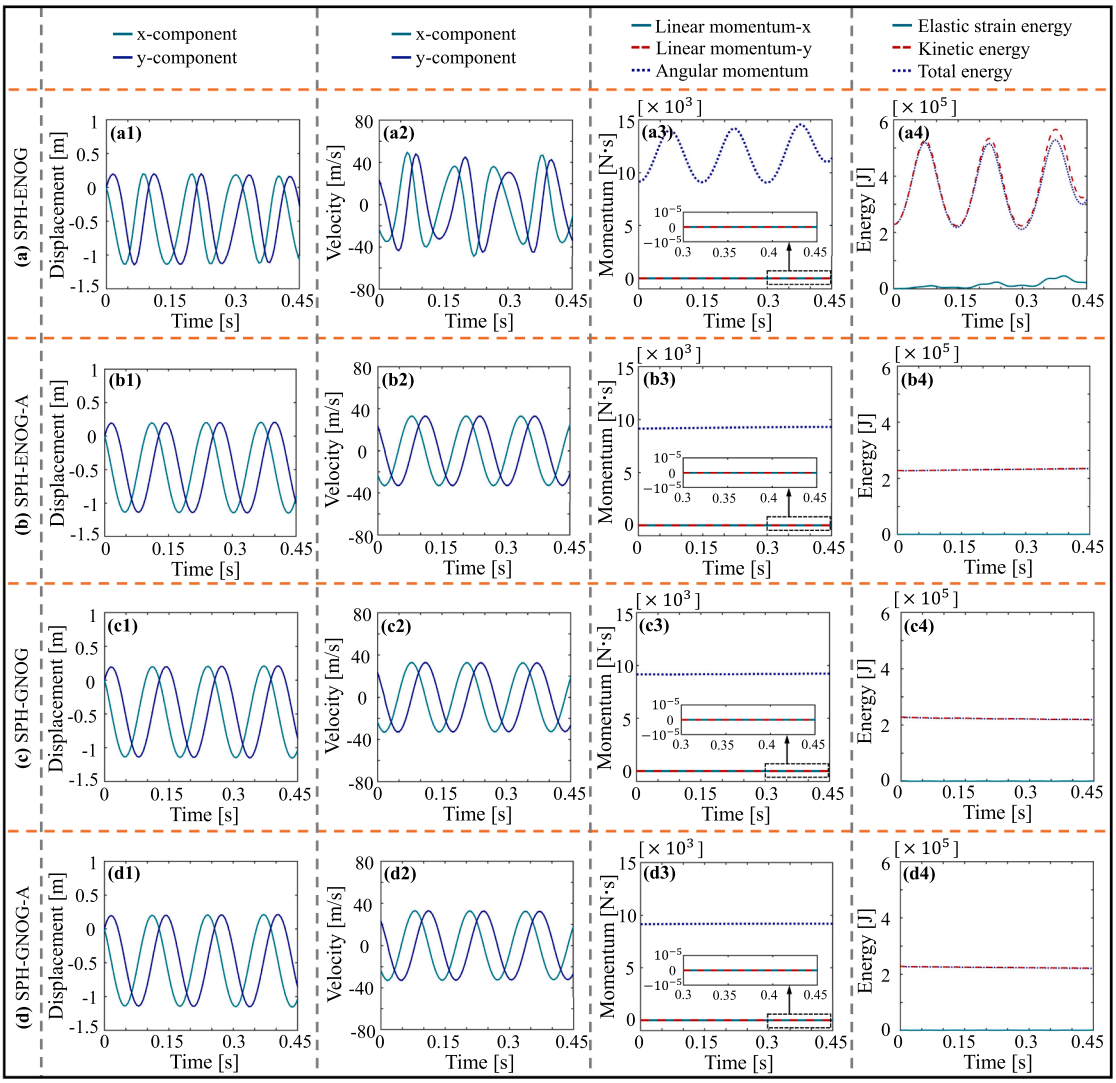

Fig. 12. 2D spinning plate: time histories of displacement and velocity at the observation point, along with linear/angular momentum and energies, for (a) SPH-ENOG [26], (b) SPH-ENOG-A, (c) SPH-GNOG [18], and (d) SPH-GNOG-A.

ulus $E = 1.7 \times 10^7$ Pa, and Poisson's ratio $\nu = 0.45$. The initial particle spacing is set to 0.05 m. An observation point is placed at the top-right corner of the plate to track the time histories of displacement and velocity.

Fig. 11 presents the temporal evolution of (a) pressure distribution from SPH-ENOG-A and (b) von Mises stress distribution from SPH-GNOG-A. The consistently negative pressure in Fig. 11a indicates a tension-dominated state throughout the plate. Both methods exhibit smooth pressure/stress profiles and maintain uniform particle distributions, with no evidence of particle clustering or numerical fractures-demonstrating that the proposed formulations effectively suppress numerical instabilities even under predominantly tensile loading conditions.

Fig. 12 provides a comprehensive comparison of the temporal evolution of displacement and velocity at the observation point, along with linear momentum, angular momentum, and energy histories, for four SPH schemes: SPH-ENOG [26], SPH-ENOG-A, SPH-GNOG [18], and SPH-GNOG-A. In the case of SPH-ENOG (row a), the velocity history (subfigure a2) exhibits noticeable fluctuations in amplitude, which can be attributed to the poor conservation of angular momentum (subfigure a3). This angular momentum non-conservation further induces unphysical oscillations in kinetic energy. When the angular-momentum enhanced SPH-ENOG-A is employed (row b), the angular momentum remains stably (subfigure b3), showing a significant enhancement compared to SPH-ENOG. Consequently, the conservation of total energy is significantly improved. For the SPH-GNOG (row c), the level of angular-momentum conservation (subfigure c3) is substantially better than that of SPH-ENOG (subfigure a3). This is because the corrective term $\widehat{\mathbf{a}}_i$ in SPH-GNOG's shear acceleration discretization (Eq. (45)) introduces only a minor perturbation to the original formulation, whereas SPH-ENOG entirely reconstructs the shear acceleration term (Eq. (25)), leading to more severe non-conservation. With the

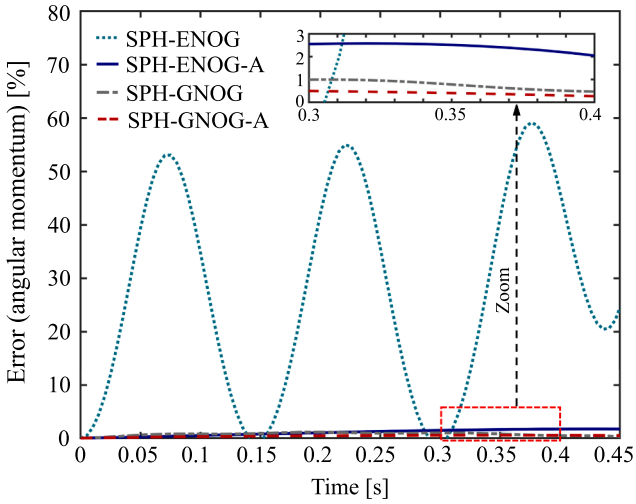

Fig. 13. 2D spinning plate: evolution of angular momentum error for different numerical schemes.

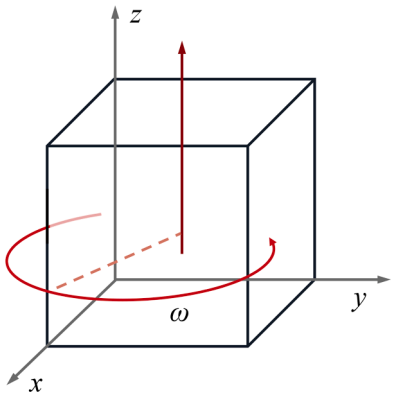

Fig. 14. 3D spinning cube: model setup.

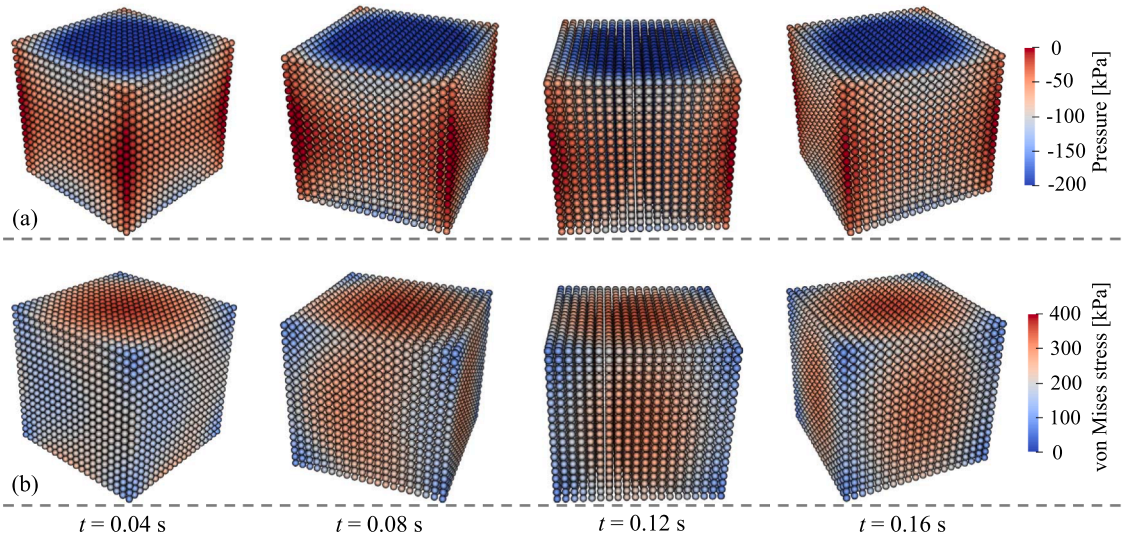

Fig. 15. 3D spinning cube: evolution of particle configuration at different instants for (a) SPH-ENOG-A, colored by pressure, and (b) SPH-GNOG-A, colored by von Mises stress.

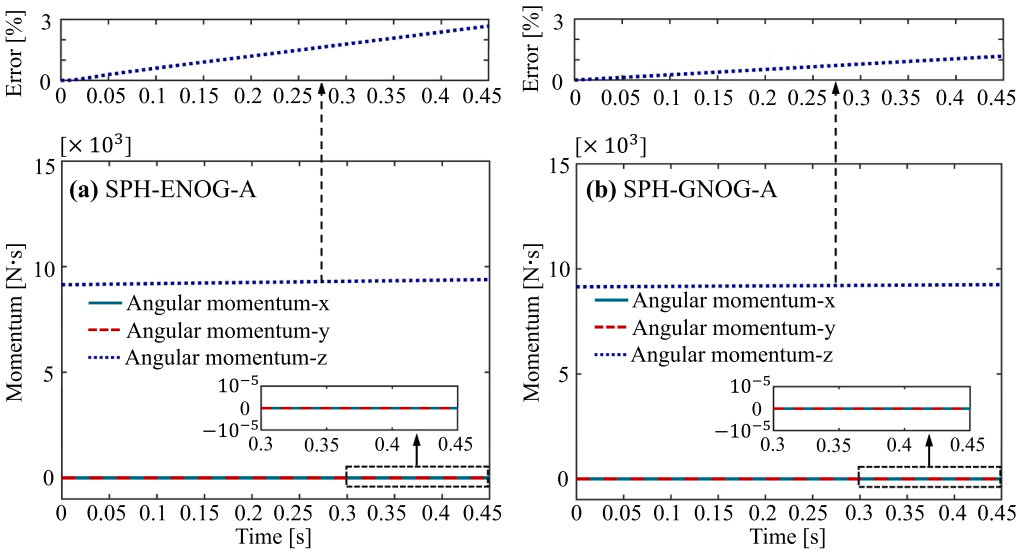

Fig. 16. 3D spinning cube: temporal evolution of angular momentum computed using (a) SPH-ENOG-A and (b) SPH-GNOG-A.

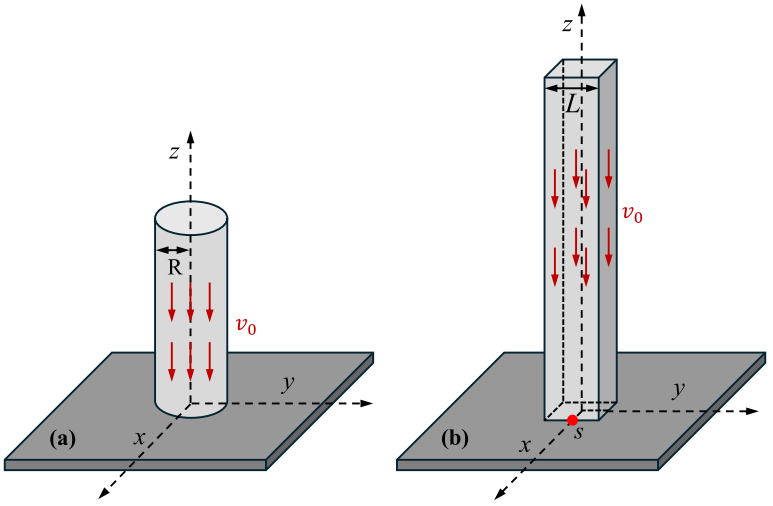

Fig. 17. Model setup for (a) round Taylor bar and (b) square Taylor bar.

introduction of SPH-GNOG-A (row d), the corrective term is reformulated to improve angular momentum conservation. Furthermore, linear momentum conservation is also maintained with high fidelity (subfigure a3-d3), demonstrating that the method successfully resolves the angular momentum issue without introducing global linear momentum drift in such standard benchmarks.

Fig. 13 quantifies the temporal evolution of the angular momentum deviation from its theoretical value across all schemes. The results clearly illustrate the enhanced performance of the new numerical treatments concerning angular momentum conservation. For materials modeled using the original SPH-ENOG scheme, a severe maximum error of 59.17% was observed. The application of the new stabilization technique in SPH-ENOG-A radically addresses this issue, slashing the peak error to a mere 2.58%. This dramatic reduction highlights the critical role of SPH-ENOG-A in ensuring robust angular momentum preservation for highly elastic simulations. Furthermore, even for the already low-error baseline provided by SPH-GNOG (maximum error 1.12%), its modified counterpart, SPH-GNOG-A, achieves a worthwhile improvement, reducing the maximum error to 0.55%. This refinement indicates that SPH-GNOG-A serves to fine-tune the accuracy of the velocity and displacement fields.

Although the improvement in angular momentum conservation achieved by SPH-GNOG-A over SPH-GNOG is modest, a consequence of the limited influence of the corrective term, its primary advantage lies in establishing a unified applicability for the modeling coefficient ξ_G across both elastic and plastic materials. In stark contrast, the original SPH-GNOG formulation necessitated the use of distinct ξ_G values for elastic and plastic materials [18]. This divergence was due to the nature of plastic deformation, which induces more irregular and complex rotations that significantly amplify the effects of angular momentum non-conservation. SPH-GNOG-A

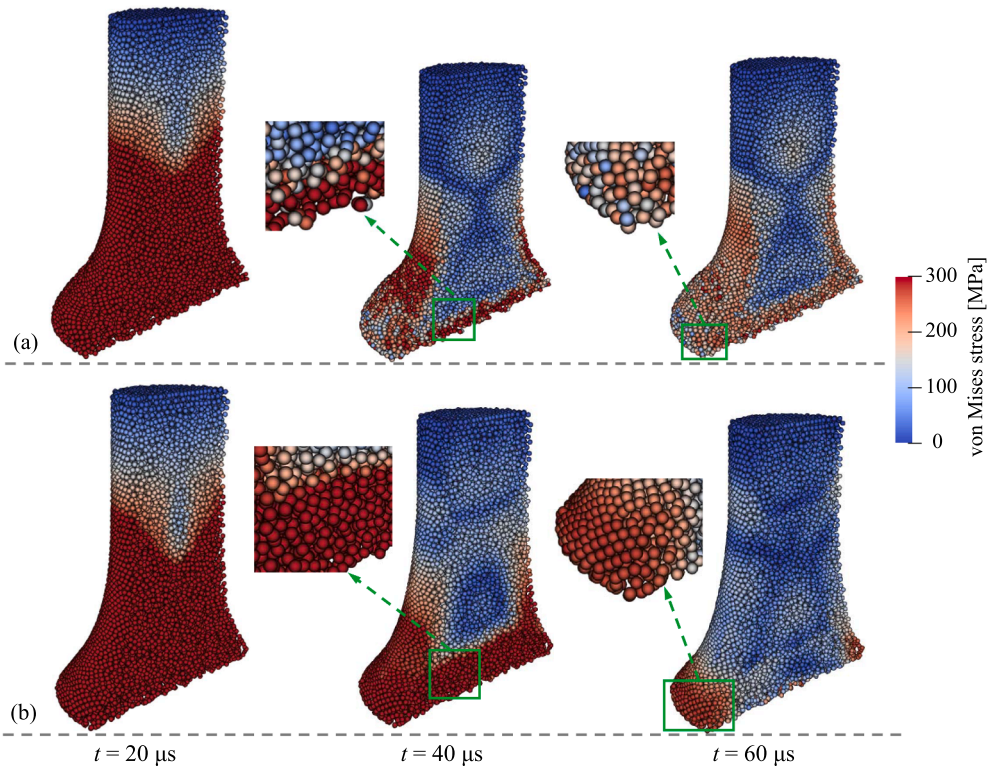

Fig. 18. Round Taylor bar: longitudinal section view showing temporal evolution of particle configurations for (a) SPH-OG [18] and (b) SPH-GNOG-A. Particles are colored by von Mises stress ($dp = R/12$).

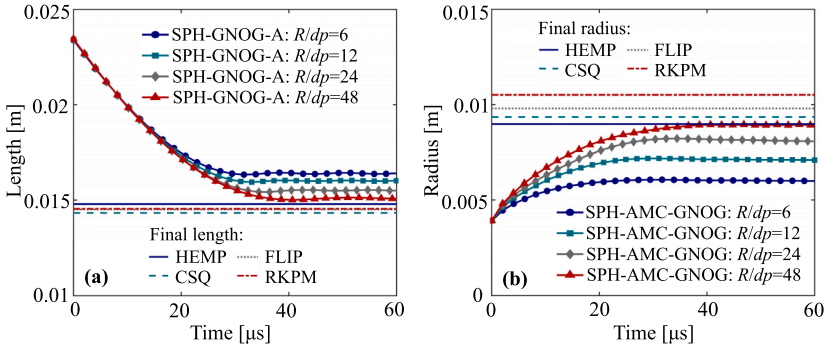

Fig. 19. Round Taylor bar: temporal evolution of (a) length and (b) radius of the bar at various resolutions. The results are compared with the final values of length and radius obtained from HEMP [59], CSQ [60], FLIP [61], and RKPM [57].

effectively eliminates this dependency, thereby guaranteeing consistent and robust computational performance irrespective of the material's mechanical state.

5.1.4. 3D spinning cube

To further assess the conservation characteristics of the proposed formulations in 3D settings, the spinning cube benchmark is employed. Adopting the configuration from Lee et al. [55], a unit-side-length cube is set in rigid-body rotation about its centroid with an angular velocity of $\omega = [0, 0, 50]^{\mathrm{T}}$ rad/s, free from external constraints or initial deformation, as illustrated in Fig. 14. This case extends the previous 2D spinning plate analysis to three dimensions, providing a more comprehensive assessment of the angular momentum conservation capabilities of SPH-ENOG-A and SPH-GNOG-A formulations. The cube is modeled as an elastic solid with the following properties [55]: density $\rho_0 = 1100\,\mathrm{kg/m^3}$, Young's modulus $E = 1.7 \times 10^7$ Pa, and Poisson's ratio $\nu = 0.3$. The discretization employs an initial particle spacing of 0.05 m.

Fig. 15 illustrates the dynamic response of the 3D spinning cube, with (a) SPH-ENOG-A depicting pressure evolution and (b) SPH-GNOG-A showing von Mises stress development. Both numerical approaches yield physically plausible results, as evidenced

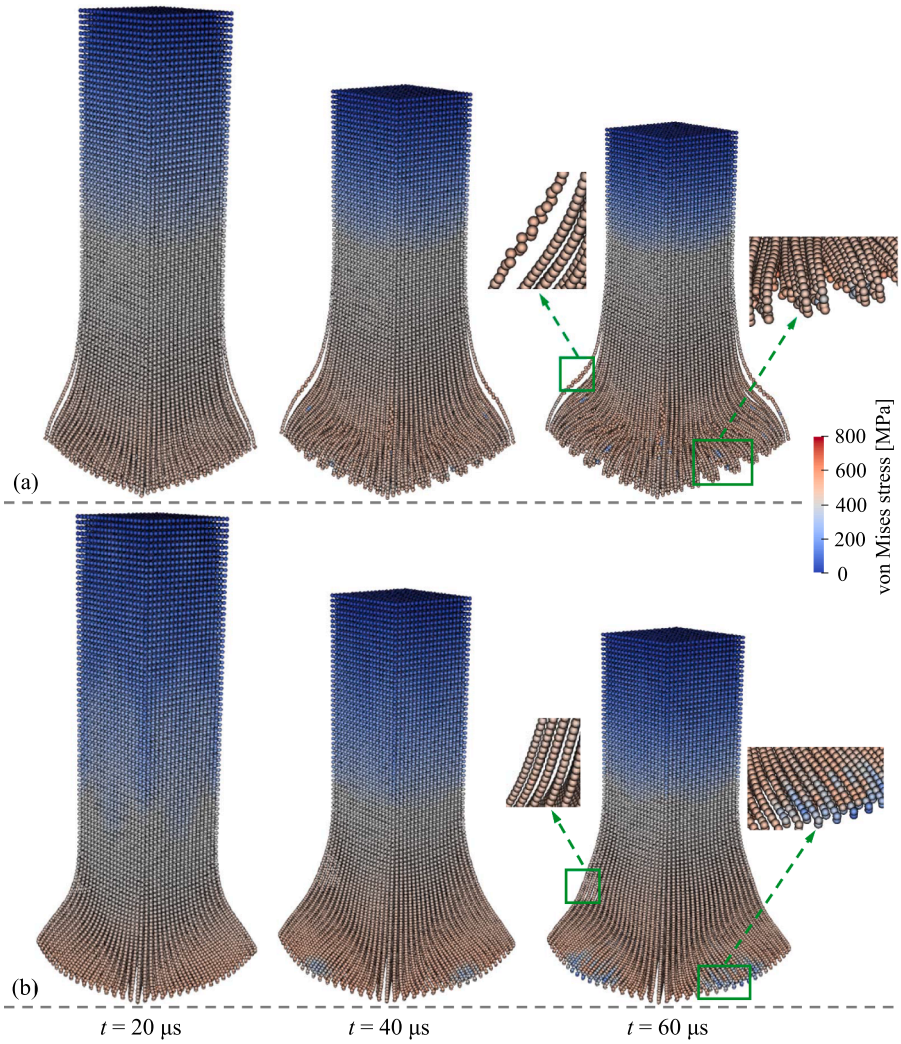

Fig. 20. Square Taylor bar: temporal evolution of particle configurations for (a) SPH-OG [18] and (b) SPH-GNOG-A. Particles are colored by von Mises stress ($dp = L/20$).

by the well-preserved particle organization and absence of stress anomalies throughout the simulation. The smooth transitions in both pressure and stress fields, coupled with maintained particle homogeneity, confirm the numerical robustness of the proposed formulations in handling 3D spinning motions. Fig. 16 compares the temporal evolution of angular momentum for the SPH-ENOG-A and SPH-GNOG-A formulations. Both exhibit superb conservation properties, with angular momentum remaining nearly constant throughout the simulation. Specifically, the maximum relative error is 2.67% for SPH-ENOG-A and 1.18% for SPH-GNOG-A.

5.2. Plastic examples

While the above numerical examples have focused on elastic materials to validate both SPH-ENOG-A and SPH-GNOG-A formulations, it is important to note that SPH-ENOG-A is restricted to elastic material modeling, whereas SPH-GNOG-A maintains unified applicability to both elastic and plastic materials. Consequently, the following cases employ a plastic benchmark to evaluate the stability and accuracy of SPH-GNOG-A. Notably, unlike the original SPH-GNOG [18] which required scaling the modeling coefficient ξ_G for plastic materials, the proposed SPH-GNOG-A enables the use of a consistent $\xi_G = 2$ value across different material types.

5.2.1. Round Taylor bar

We now consider a classic impact problem originally introduced by Taylor [56] to measure yield properties, which has been widely adopted for validating elastoplastic material models [57,58]. As illustrated in Fig. 17a, a cylindrical bar with an initial radius $R = 3.91 \times 10^{-3}$ m and length 2.346×10^{-2} m impacts a rigid frictionless wall with an initial velocity $\mathbf{v}_0 = (0, 0, -373)$ m/s. The simulation begins at $t = 0$ when the bar first contacts the wall. Material response is described by a J_2 model with perfect plasticity [57], using

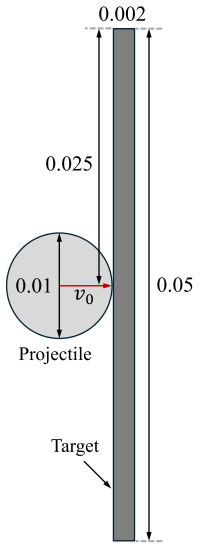

Fig. 21. High-velocity impact: model setup (unit: m).

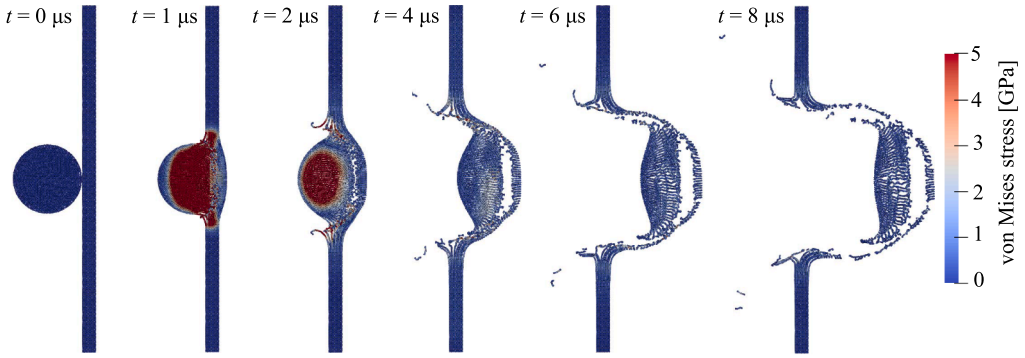

Fig. 22. High-velocity impact: evolution of von Mises stress with the present SPH-GNOG-A at different times.

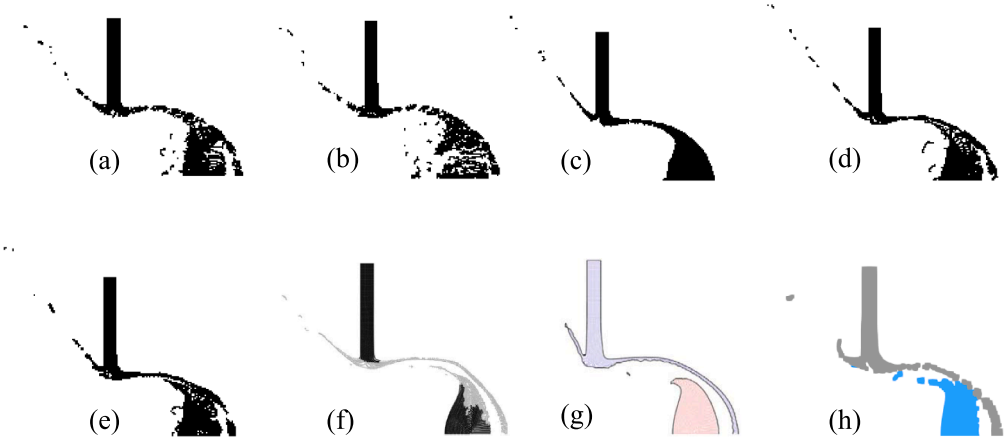

Fig. 23. High-velocity impact: deformation of projectile and target at $t = 8\mu s$ obtained with different algorithms, i.e., (a) BAL [64], (b) MON [64], (c) CON [64], (d) SAV1 [64], (e) SAV2 [64], (f) adaptive total Lagrangian Eulerian SPH [65], (g) Xiao and Liu's study [66], and (h) the present SPH-GNOG-A.

Table 4
Square Taylor bar: the x-coordinate of the observation point s at the final moment ($t = 60\mu$s).

	$L/dp = 8$	$L/dp = 12$	$L/dp = 16$	$L/dp = 20$	Haider et al. [62]
x-coordinate (mm)	5.21	5.91	6.46	6.86	6.93

the following parameters [57]: density $\rho_0 = 2700\,\mathrm{kg/m^3}$, Young's modulus $E = 7.82 \times 10^{10}$ Pa, Poisson's ratio $\nu = 0.3$, and yield stress $\sigma_Y = 2.9 \times 10^8$ Pa.

Fig. 18 displays particle configurations (longitudinal section) during the impact of a cylindrical Taylor bar. Results are reported for SPH-OG [18] (Fig. 18a) and for the proposed SPH-GNOG-A formulation (Fig. 18b). Owing to the bar's axisymmetric geometry and the initially isotropic particle distribution, both methods preserve a largely uniform particle arrangement. However, SPH-OG yields noticeably non-smooth von Mises stress fields, whereas SPH-GNOG-A produces smoother stress distributions with minimal numerical artifacts across the domain, indicating effective suppression of hourglass modes under plastic deformation. Fig. 19 quantifies the time evolution of the bar length and radius at multiple spatial resolutions. Dotted curves correspond to SPH-GNOG-A at different discretization levels, while solid lines denote reference solutions from established methods, including HEMP [59], CSQ [60], FLIP [61], and RKPM [57]. The SPH-GNOG-A solutions converge toward the published benchmarks as the resolution increases, thereby confirming both the accuracy and the spatial convergence properties of the proposed formulation.

5.2.2. Square Taylor bar

This subsection extends the Taylor bar impact analysis to a square cross-section geometry, providing an additional benchmark for evaluating the proposed formulations under more complex stress states. As depicted in Fig. 17b, a square bar with initial height $H = 0.03$ m and cross-sectional side length $L = 0.006$ m impacts a rigid wall with initial velocity $\mathbf{v}_0 = (0, 0, -227)$ m/s, following the configuration established in [62]. An observation point is positioned at coordinates $(0.003, 0, 0)$ m to track displacement history during deformation. Material behavior is modeled using a J_2 plasticity framework incorporating linear isotropic hardening [62]. The constitutive parameters are specified as follows: density $\rho_0 = 8930\,\mathrm{kg/m^3}$, Young's modulus $E = 1.17 \times 10^{11}$ Pa, Poisson's ratio $\nu = 0.35$, initial yield stress $\sigma_Y = 4 \times 10^8$ Pa, and hardening modulus $\kappa = 1 \times 10^8$ Pa. This configuration introduces distinct corner effects and stress concentration patterns compared to the cylindrical Taylor bar case, offering enhanced validation of the algorithm's capability to handle complex plastic flow geometries.

Fig. 20 compares the deformation patterns of the square Taylor bar simulated using SPH-OG and the proposed SPH-GNOG-A formulation, with particle configurations colored by von Mises stress. The SPH-OG results exhibit pronounced particle disordering, while SPH-GNOG-A maintains coherent particle arrangements throughout the impact process, demonstrating enhanced numerical stability in handling severe plastic deformation. Convergence analysis is quantitatively assessed in Table 4, which presents the final x-coordinate of observation point s at various spatial resolutions. The SPH-GNOG-A results show systematic convergence toward the reference solution by Haider et al. [62] as resolution increases, with the finest discretization ($L/dp = 20$) achieving close agreement. This consistent convergence behavior validates the accuracy and robustness of the proposed formulation for impact problems involving complex plastic flow.

5.2.3. High-velocity impact

This section examines a challenging high-velocity impact scenario involving a circular projectile striking a rectangular target, building upon previous investigations [63,64]. The simulation is designed to evaluate the capability of the proposed formulation to handle extreme deformation and material fragmentation under dynamic loading conditions. As shown in Fig. 21, the configuration consists of a circular projectile with a diameter of 0.01 m impacting a rectangular target of dimensions 0.05 m (height) × 0.002 m (width) at an initial velocity of $v_0 = 3100$ m/s [64], with the target being unconstrained. Both components are modeled as aluminum with elastic-perfectly plastic material response. Following established parameters from prior studies [64,65], the material properties are specified as: density $\rho_0 = 8930\,\mathrm{kg/m^3}$, Young's modulus $E = 7.417 \times 10^{10}\,\mathrm{N/m^2}$, Poisson's ratio $\nu = 0.344$, sound speed $c_0 = 5328$ m/s, and yield stress $\sigma_Y = 3 \times 10^8\,\mathrm{N/m^2}$. The initial particle spacing is set to $dp = 0.0002$ m.

The dynamic response during high-velocity impact is captured in Fig. 22, which illustrates the temporal progression of von Mises stress distribution using the proposed SPH-GNOG-A formulation. Notably, the stress field maintains smooth transitions without exhibiting hourglass patterns, confirming the method's robustness under extreme loading conditions. Fig. 23 compares deformation patterns at $t = 8\mu$s obtained using various numerical approaches, including multiple SPH variants from the literature and the present SPH-GNOG-A. The proposed method produces deformation morphologies consistent with established schemes.

6. Conclusions and outlook

This paper introduces two angular-momentum-enhanced formulations for SPH solid dynamics: SPH-ENOG-A for elastic materials and SPH-GNOG-A with unified applicability to both elastic and plastic materials. A central contribution is the incorporation of Rodrigues' rotation matrices to explicitly track finite rotational motions, thereby ensuring angular momentum enhancement. Strict conservation of linear momentum is achieved by calculating the average rotation matrix at each time step and applying it uniformly to all particles. Although this approach introduces a minor compromise in angular momentum conservation, the improvement achieved is still substantially better than in prior versions.

The numerical studies support the following conclusions:

- Performance in elastic benchmarks: Both SPH-ENOG-A and SPH-GNOG-A exhibit excellent stability and accuracy in classical elastic tests (e.g., oscillating plates), while fully preserving the hourglass-suppression capabilities of their predecessors.
- Angular momentum enhancement: By introducing a rotation-corrected formulation, the proposed methods achieve a marked improvement in angular momentum conservation, which translates to more accurate and stable results in rotation-dominated scenarios. In the spinning plate test, SPH-ENOG-A significantly reduces the maximum angular momentum error from 59.17% (in SPH-ENOG) to 2.58%. Similarly, SPH-GNOG-A reduces the maximum error relative to SPH-GNOG from 1.12% to 0.55%. This demonstrates that while SPH-ENOG-A substantially enhances angular-momentum conservation for elastic materials, SPH-GNOG-A further refines the already low error of SPH-GNOG, ensuring highly accurate displacement and velocity predictions in problems with significant rotational components.
- Unified material modeling: Although the gain in angular momentum conservation from SPH-GNOG-A over SPH-GNOG is modest-because the hourglass control term in SPH-GNOG operates primarily as a corrective term with limited influence-a key advancement is the ability of SPH-GNOG-A to use a single parameter setting ($\xi_G = 2$) for both elastic and plastic materials. This removes the material-dependent parameter in SPH-GNOG and substantially enhances the practical utility of the method for industrial applications involving complex material responses.
- Plastic deformation capability: SPH-GNOG-A demonstrates robust performance in challenging plastic impact problems, including Taylor bar and high-velocity impact scenarios. It maintains smooth stress fields and coherent particle distributions under severe plastic deformation, confirming its suitability for a broad range of engineering applications.
- Limitations and future work: Despite these advances, several research directions remain. Incorporating more sophisticated constitutive models-such as those accounting for damage and fracture-would broaden the method's applicability. Extending the approach to fluid-structure interaction and developing adaptive resolution strategies could further improve computational efficiency for large-scale simulations.

In summary, SPH-ENOG-A and SPH-GNOG-A address fundamental limitations of existing SPH formulations for solid dynamics. By significantly enhancing angular momentum conservation and retaining strong stability properties, they offer reliable tools for simulating complex solid mechanics across elastic and plastic regimes.

CRediT authorship contribution statement

Shuaihao Zhang: Writing – original draft, Visualization, Validation, Methodology, Investigation, Formal analysis, Conceptualization; **Jidong Zhao:** Writing – review & editing, Supervision, Funding acquisition; **Honghu Zhu:** Writing – review & editing, Investigation; **Xiangyu Hu:** Writing – review & editing, Supervision, Funding acquisition, Formal analysis, Conceptualization.

Data availability

The code is available as open-source through the SPHinXsys project: https://www.sphinxsys.org.

Declaration of competing interest

The authors declare that they have no known competing financial interests or personal relationships that could have appeared to influence the work reported in this paper.

Acknowledgements

This work is financially supported by the German Research Foundation (DFG HU1527/12-4), and the Research Grants Council of Hong Kong (TRS #T22-607/24N).

References

[1] L.B. Lucy, A numerical approach to the testing of the fission hypothesis, Astron. J. 82 (1977) 1013–1024.
[2] R.A. Gingold, J.J. Monaghan, Smoothed particle hydrodynamics: theory and application to non-spherical stars, Mon. Not. R. Astron. Soc. 181 (3) (1977) 375–389.
[3] J.P. Morris, P.J. Fox, Y. Zhu, Modeling low reynolds number incompressible flows using SPH, J. Comput. Phys. 136 (1) (1997) 214–226.
[4] M. Luo, C.G. Koh, W. Bai, M. Gao, A particle method for two-phase flows with compressible air pocket, Int. J. Numer. Methods Eng. 108 (7) (2016) 695–721.
[5] D.J. Price, Smoothed particle hydrodynamics and magnetohydrodynamics, J. Comput. Phys. 231 (3) (2012) 759–794.
[6] S. Zhang, S.D.N. Lourenço, X. Hu, Multiphase SPH for surface tension: resolving zero-surface-energy modes and achieving high reynolds number simulations, Comput. Methods Appl. Mech. Eng. 444 (2025) 118147.
[7] J.P. Gray, J.J. Monaghan, R. Swift, SPH Elastic dynamics, Comput. Methods Appl. Mech. Eng. 190 (49–50) (2001) 6641–6662.
[8] G.R. Johnson, R.A. Stryk, S.R. Beissel, SPH For high velocity impact computations, Comput. Methods Appl. Mech. Eng. 139 (1–4) (1996) 347–373.
[9] J.-Y. Chen, X.-Z. Song, C. Peng, A coupled FD-SPH framework for the damage evaluation of ceramic-steel composite structures subjected to blast loading, Comput. Struct. 309 (2025) 107653.
[10] J.-Y. Chen, J. Zhao, R.-F. Feng, R.-C. Ni, C. Peng, Coupled FDM-SPH modeling of CFRP-reinforced concrete damage under combined blast and fragment impact, Comput. Struct. 319 (2025) 107980.
[11] J.-Y. Chen, J. Zhao, R.-F. Feng, R.-C. Ni, C. Peng, GPU-Accelerated multi-material FVM–SPH with immersed boundary method for high-fidelity modeling of shock–structure interactions, Comput. Mech. (2025) 1–23.
[12] S. Zhang, D. Wu, X. Hu, C.E. Choi, S.D.N. Lourenço, An efficient SPH framework for modeling binary granular mixtures and implications for granular flows, Int. J. Numer. Anal. Methods Geomech. 49 (3) (2025) 815–838.

[13] R. Feng, J. Zhao, G. Fourtakas, B.D. Rogers, GeoDualSPHysics: a high-performance SPH solver for large deformation modelling of geomaterials with two-way coupling to multi-body systems, Comput. Phys. Commun. 320 (2026) 109965.
[14] C. Antoci, M. Gallati, S. Sibilla, Numerical simulation of fluid–structure interaction by SPH, Comput. Struct. 85 (11–14) (2007) 879–890.
[15] A. Khayyer, H. Gotoh, Y. Shimizu, Y. Nishijima, A 3D lagrangian meshfree projection-based solver for hydroelastic fluid-Structure interactions, J. Fluids Struct. 105 (2021) 103342.
[16] A. Khayyer, H. Gotoh, H. Falahaty, Y. Shimizu, An enhanced ISPH–SPH coupled method for simulation of incompressible fluid–elastic structure interactions, Comput. Phys. Commun. 232 (2018) 139–164.
[17] S.-C. Hwang, A. Khayyer, H. Gotoh, J.-C. Park, Development of a fully lagrangian MPS-based coupled method for simulation of fluid–structure interaction problems, J. Fluids Struct. 50 (2014) 497–511.
[18] S. Zhang, D. Wu, S.D.N. Lourenço, X. Hu, A generalized non-hourglass updated lagrangian formulation for SPH solid dynamics, Comput. Methods Appl. Mech. Eng. 440 (2025) 117948.
[19] J.J. Monaghan, SPH Without a tensile instability, J. Comput. Phys. 159 (2) (2000) 290–311.
[20] J.W. Swegle, D.L. Hicks, S.W. Attaway, Smoothed particle hydrodynamics stability analysis, J. Comput. Phys. 116 (1) (1995) 123–134.
[21] A.G. Petschek, M.E. Hanson, Difference equations for two-dimensional elastic flow, J. Comput. Phys. 3 (2) (1968) 307–321.
[22] T.B. Belytschko, et al., Finite element approach to hydrodynamics and mesh stabilization, Computation Methods in Nonlinear Mechanics, ed. Oden, JT et al. The Texas Institute for Computational Mechanics (1974).
[23] G.C. Ganzenmüller, An hourglass control algorithm for lagrangian smooth particle hydrodynamics, Comput. Methods Appl. Mech. Eng. 286 (2015) 87–106.
[24] D. Wu, C. Zhang, X. Tang, X. Hu, An essentially non-hourglass formulation for total lagrangian smoothed particle hydrodynamics, Comput. Methods Appl. Mech. Eng. 407 (2023) 115915.
[25] R. Vignjevic, J. Campbell, L. Libersky, A treatment of zero-energy modes in the smoothed particle hydrodynamics method, Comput. Methods Appl. Mech. Eng. 184 (1) (2000) 67–85.
[26] S. Zhang, S.D.N. Lourenço, D. Wu, C. Zhang, X. Hu, Essentially non-hourglass SPH elastic dynamics, J. Comput. Phys. (2024) 113072.
[27] R. Vignjevic, J. Campbell, Review of development of the smooth particle hydrodynamics (SPH) method, in: Predictive Modeling of Dynamic Processes: A Tribute to Professor Klaus Thoma, Springer, 2009, pp. 367–396.
[28] C. Zhang, M. Rezavand, Y. Zhu, Y. Yu, D. Wu, W. Zhang, J. Wang, X. Hu, SPHinXsys: an open-source multi-physics and multi-resolution library based on smoothed particle hydrodynamics, Comput. Phys. Commun. 267 (2021) 108066.
[29] R.I. Borja, Plasticity, Springer, Berlin Heidelberg 10 (2013) 978–983.
[30] E.W.V. Chaves, Notes on continuum mechanics, Springer Science & Business Media, 2013.
[31] J.C. Simo, T.J.R. Hughes, Computational inelasticity, 7, Springer Science & Business Media, 2006.
[32] C. Zhang, X.Y. Hu, N.A. Adams, A weakly compressible SPH method based on a low-dissipation riemann solver, J. Comput. Phys. 335 (2017) 605–620.
[33] S. Zhang, C. Zhang, X. Hu, S.D.N. Lourenço, A riemann-based SPH method for modelling large deformation of granular materials, Comput. Geotech. 167 (2024) 106052.
[34] P. Espanol, M. Revenga, Smoothed dissipative particle dynamics, Phys. Rev. E 67 (2) (2003) 026705.
[35] P.W. Randles, L.D. Libersky, Smoothed particle hydrodynamics: some recent improvements and applications, Comput. Methods Appl. Mech. Eng. 139 (1–4) (1996) 375–408.
[36] J. Bonet, S. Kulasegaram, A simplified approach to enhance the performance of smooth particle hydrodynamics methods, Appl. Math. Comput. 126 (2–3) (2002) 133–155.
[37] C. Zhang, M. Rezavand, X. Hu, Dual-criteria time stepping for weakly compressible smoothed particle hydrodynamics, J. Comput. Phys. 404 (2020) 109135.
[38] C. Zhang, M. Rezavand, X. Hu, A multi-resolution SPH method for fluid-structure interactions, J. Comput. Phys. 429 (2021) 110028.
[39] S. Zhang, Stability-Enhanced Smoothed Particle Hydrodynamics for Geomaterials: Methods and Applications, (Thesis), The University of Hong Kong, Pokfulam, Hong Kong SAR, 2025.
[40] X.Y. Hu, N.A. Adams, Angular-momentum conservative smoothed particle dynamics for incompressible viscous flows, Phys. Fluids 18 (10) (2006).
[41] K.M. Lynch, F.C. Park, Modern robotics, Cambridge University Press, 2017.
[42] O. Rodrigues, Des lois géométriques qui régissent les déplacements d'un système solide dans l'espace, et de la variation des coordonnées provenant de ces déplacements considérés indépendamment des causes qui peuvent les produire, J. Mathématiques Pures Appliquées 5 (1840) 380–440.
[43] H. Wendland, Piecewise polynomial, positive definite and compactly supported radial functions of minimal degree, Adv. Comput. Math. 4 (1995) 389–396.
[44] Y. Shimizu, A. Khayyer, H. Gotoh, An implicit SPH-based structure model for accurate fluid–structure interaction simulations with hourglass control scheme, Eur. J. Mech.-B/Fluids 96 (2022) 122–145.
[45] D. Wu, X. Tang, S. Zhang, X. Hu, Unified non-hourglass formulation for total lagrangian SPH solid dynamics, Comput. Mech. 75 (3) (2025) 1081–1113.
[46] S. Zhang, F. Wang, X. Hu, S.D.N. Lourenço, A unified transport-velocity formulation for SPH simulation of cohesive granular materials, Comput. Geotech. 181 (2025) 107139.
[47] L.D. Landau, E.M. Lifshitz, Course of theoretical physics, Elsevier, 2013.
[48] C. Zhang, X.Y. Hu, N.A. Adams, A generalized transport-velocity formulation for smoothed particle hydrodynamics, J. Comput. Phys. 337 (2017) 216–232.
[49] A.W. Leissa, Vibration of plates, 160, Scientific and Technical Information Division, National Aeronautics and Space Administration, 1969.
[50] C.H. Lee, P.R. Refachinho de Campos, A.J. Gil, M. Giacomini, J. Bonet, An entropy-stable updated reference lagrangian smoothed particle hydrodynamics algorithm for thermo-elasticity and thermo-visco-plasticity, Comput. Part. Mech. 10 (6) (2023) 1493–1531.
[51] C.H. Lee, A.J. Gil, P.R.R. de Campos, J. Bonet, T. Jaugielavičius, S. Joshi, C. Wood, A novel arbitrary lagrangian eulerian smooth particle hydrodynamics algorithm for nonlinear solid dynamics, Comput. Methods Appl. Mech. Eng. 427 (2024) 117055.
[52] T.B.J. Di Giusto, C.H. Lee, A.J. Gil, J. Bonet, C. Wood, M. Giacomini, A first-order hyperbolic arbitrary lagrangian eulerian conservation formulation for nonlinear solid dynamics in irreversible processes, J. Comput. Phys. 518 (2024) 113322.
[53] A. Khayyer, Y. Shimizu, C.H. Lee, A. Gil, H. Gotoh, J. Bonet, An improved updated lagrangian SPH method for structural modelling, Comput. Part. Mech. 11 (3) (2024) 1055–1086.
[54] C.H. Lee, A.J. Gil, J. Bonet, Development of a cell centred upwind finite volume algorithm for a new conservation law formulation in structural dynamics, Comput. Struct. 118 (2013) 13–38.
[55] C.H. Lee, A.J. Gil, G. Greto, S. Kulasegaram, J. Bonet, A new jameson–Schmidt–Turkel smooth particle hydrodynamics algorithm for large strain explicit fast dynamics, Comput. Methods Appl. Mech. Eng. 311 (2016) 71–111.
[56] G.I. Taylor, The use of flat-ended projectiles for determining dynamic yield stress i. theoretical considerations, Proceedings of the Royal Society of London. Series A. Mathematical and Physical Sciences 194 (1038) (1948) 289–299.
[57] J.-S. Chen, C. Pan, C.-T. Wu, W.K. Liu, Reproducing kernel particle methods for large deformation analysis of non-linear structures, Comput. Methods Appl. Mech. Eng. 139 (1–4) (1996) 195–227.
[58] C.H. Lee, A.J. Gil, J. Bonet, Development of a stabilised petrov–Galerkin formulation for conservation laws in lagrangian fast solid dynamics, Comput. Methods Appl. Mech. Eng. 268 (2014) 40–64.
[59] M.L. Wilkins, M.W. Guinan, Impact of cylinders on a rigid boundary, J. Appl. Phys. 44 (3) (1973) 1200–1206.
[60] W.W. Predebon, C.E. Anderson, Jr, J.D. Walker, Inclusion of evolutionary damage measures in eulerian wavecodes, Comput. Mech. 7 (4) (1991) 221–236.
[61] D. Sulsky, S.-J. Zhou, H.L. Schreyer, Application of a particle-in-cell method to solid mechanics, Comput. Phys. Commun. 87 (1–2) (1995) 236–252.
[62] J. Haider, C.H. Lee, A.J. Gil, J. Bonet, A first-order hyperbolic framework for large strain computational solid dynamics: an upwind cell centred total lagrangian scheme, Int. J. Numer. Methods Eng. 109 (3) (2017) 407–456.
[63] B.P. Howell, G.J. Ball, A free-Lagrange augmented godunov method for the simulation of elastic–plastic solids, J. Comput. Phys. 175 (1) (2002) 128–167.

[64] V. Mehra, S. Chaturvedi, High velocity impact of metal sphere on thin metallic plates: a comparative smooth particle hydrodynamics study, J. Comput. Phys. 212 (1) (2006) 318–337.
[65] J. Young, F. Teixeira-Dias, A. Azevedo, F. Mill, Adaptive total lagrangian eulerian SPH for high-velocity impacts, Int. J. Mech. Sci. 192 (2021) 106108.
[66] Y. Xiao, K. Liu, Penalty-based surface-to-surface contact algorithm for SPH method, Appl. Math. Model. 117 (2023) 359–377.